Weighted Nonlocal Low-Rank Tensor Decomposition Method for Sparse Unmixing of Hyperspectral Images

Le Sun, *Member, IEEE*, Feiyang Wu, Tianming Zhan, *Member, IEEE*, Wei Liu, Jin Wang, and Byeungwoo Jeon, *Senior Member, IEEE*

***Abstract*—The low spatial resolution of hyperspectral images leads to the coexistence of multiple ground objects in a single pixel (called mixed pixels). A large number of mixed pixels in a hyperspectral image hinders the subsequent analysis and application of the image. In order to solve this problem, a novel sparse unmixing method, which considers highly similar patches in nonlocal regions of a hyperspectral image, is proposed in this article. This method exploits spectral correlation by using collaborative sparsity regularization and spatial information by employing total variation and weighted nonlocal low-rank tensor regularization. To effectively utilize the tensor decomposition, nonlocal similar patches are first grouped together. Then, these nonlocal patches are stacked to form a patch group tensor. Finally, weighted low-rank tensor regularization is enforced to constrain the patch group to obtain an estimated low-rank abundance image. Experiments on simulated and real hyperspectral datasets validated the superiority of the proposed method in better maintaining fine details and obtaining better unmixing results.**

***Index Terms*—Low-rank, nonlocal similarity, sparse unmixing, tensor decomposition.**

Manuscript received December 21, 2019; revised January 15, 2020 and February 18, 2020; accepted March 11, 2020. Date of publication March 13, 2020; date of current version April 10, 2020. This work was supported in part by the Natural Science Foundation of China under Grants 61971233, 61672291, 61972206, and 61672293, in part by the Engineering Research Center of Digital Forensics, Ministry of Education, and in part by PAPD fund. *(Corresponding author: Tianming Zhan.)*

Le Sun is with the School of Computer and Software, Nanjing University of Information Science and Technology (NUIST), Nanjing 210044, China, also with the Jiangsu Collaborative Innovation Center of Atmospheric Environment and Equipment Technology, NUIST, Nanjing 210044, China, and also with the Key Laboratory of Intelligent Perception and Systems for High-Dimensional Information of Ministry of Education, NUIST, Nanjing 210094, China (e-mail: sunlecncom@nuist.edu.cn).

Feiyang Wu is with the School of Computer and Software, Nanjing University of Information Science and Technology, Nanjing 210044, China (e-mail: feiyangwu@nuist.edu.cn).

Tianming Zhan is with the School of Information Engineering, Nanjing Audit University, Nanjing 211815, China (e-mail: ztm@nau.edu.cn).

Wei Liu is with the School of Information and Engineering, Yangzhou University, Yangzhou 225009, China (e-mail: weiliu@yzu.edu.cn).

Jin Wang is with the School of Computer and Communication Engineering, Changsha University of Science and Technology, Changsha 410114, China (e-mail: jinwang@csust.edu.cn).

Byeungwoo Jeon is with the School of Electric and Electronic Engineering, Sungkyunkwan University, Seoul 22201, South Korea (e-mail: bjeon@skku.edu).

Digital Object Identifier 10.1109/JSTARS.2020.2980576

I. Introduction

A hyperspectral image (HSI) is a three-dimensional (3-D) data cube composed of tens or even hundreds of continuous bands, with wavelengths ranging from 400 to 2500 nm. Each pixel in the HSI can be regarded as a continuous spectral signature, thus the HSI has a high spectral resolution (usually less than 10 nm) [1]. With such characteristics, HSI has been widely used in various fields, such as mineral exploration and military target identification [2]–[4]. However, multiple ground objects coexist in a single pixel (called a mixed pixel) of the HSI [5] due to the low spatial resolution, which severely impacts the precision of the subsequent HSI processing. It is important to extract the spectrum of each ground object from the mixed pixel and to obtain the corresponding abundance coefficients. That is, each mixed pixel is decomposed into products of different pure spectra (called endmembers) [6] and their corresponding proportions (called abundance coefficients) [7]. To solve the unmixing problem, two main basic models, the linear mixture model (LMM) [8]–[10] and nonlinear mixture model [11]–[14], are widely used. The LMM assumes that a linear mixture of pure endmembers can represent the observed spectral signature of each mixed pixel. Because the LMM has simplicity and clear physical meaning, it is widely used for hyperspectral unmixing.

With the LMM, the traditional endmember extraction methods are based on statistical and geometrical techniques. Although these methods, such as the pixel purity index [15] and vertex component analysis [16], require only minimal prior information about the HSI, they assume the existence of pure pixels, which is not true for most scenes. To overcome this disadvantage, methods that do not involve the assumption of pure pixel existence, such as iterative constrained endmembers [17], have been proposed and have achieved great progress. In addition, some researchers have proposed support vector machine methods [18]–[20], convolutional neural network methods [21]–[29], and nonnegative matrix factorization (NMF) methods [30]–[32] for hyperspectral unmixing. However, the support vector machine and convolutional neural network methods have shown poor unmixing performance and have even failed to unmix in instances with strong noise. The limitation of the NMF methods is that they are the nonconvex problems, and may obtain virtual endmembers that have no physical meaning.

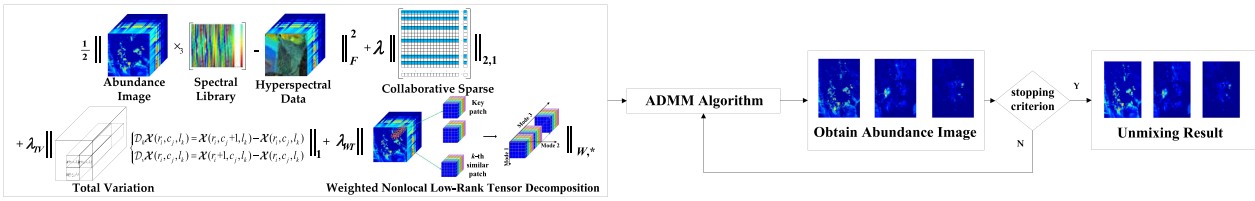

Fig. 1. Flow chart of the proposed WNLTDSU method.

To overcome these drawbacks according to compressive sensing theory [33]–[35], sparse unmixing techniques use a known spectral library to compose the endmember matrix instead of extracting endmembers from the HSI and then estimate the corresponding abundance coefficients. To obtain precise results, some prior knowledge is introduced into the sparse unmixing model, such as the abundance nonnegativity constraint (ANC) [36], abundance sum-to-one constraint [37], and sparseness of abundance [38]. The variable splitting and augmented Lagrangian for sparse unmixing (SUnSAL) [39] is a typical sparse unmixing method. They used the l_1 norm to describe sparsity. In order to enhance the sparsity of the spectrum, the collaborative SUnSAL (CLSUnSAL) method [40] indicates whether the spectrum of mixed pixels in homogeneous regions have high similarity and whether the corresponding abundance vectors have a high correlation. This prior can be expressed by applying the $l_{2,1}$ norm constraint to the abundance matrix. In addition, Deng *et al.* [41] used smooth l_0 sparse regularization and Sun *et al.* [42] utilized $l_{1/2}$ sparse regularization for hyperspectral unmixing, respectively, which characterizes the sparsity of abundance better than the l_1 norm. However, these methods ignore the spatial information in the HSI, such as the spatial distribution of pixels and the correlation between adjacent pixels [43], [44].

To account for the local spatial correlation, many sparse unmixing methods add total variation (TV) regularization to promote local smoothness in the spatial domain [45]–[47]. To explore nonlocal spatial information, many sparse unmixing methods use a nonlocal means of regularization to maintain similar spatial structure information in the HSI [48]–[50].

For the past few years, the low-rank property of the HSI has been widely used in the fields of denoising, restoration, and classification, which has achieved superior results [51]–[59]. Rizkinia *et al.* [60] converted the abundance matrix to 3-D and exploited low-rank attributes in the local region by using a local patch. Zhang *et al.* [61] proposed a low-rank representation and spectral library pruning method based on the assumption that adjacent pixels have similar abundance coefficients, and the abundance coefficients of the ground objects have small values. Hong *et al.* [62] utilized a subspace with a low-rank attribute embedding method to improve the unmixing results.

Nevertheless, the unmixing methods discussed above do not use spatial and spectral information fully, and HSI unmixing performance still needs to be improved. In the spatial domain, the pixels in a local region usually contains the same or similar materials. In an HSI, there are many such local regions with similar characteristics. That is to say, HSI has a strong nonlocal similarity [63], [64]. Based on this prior, a weighted nonlocal low-rank tensor decomposition method for HSI sparse unmixing (WNLTDSU) is proposed in this study. Fig. 1 presents the flow chart for the WNLTDSU. Given a 3-D abundance HSI image, a 3-D local patch is first utilized to slide across all dimensions of the HSI. For the local patch, similar patches are searched for in a sufficiently large enough local window of the image (in practice, usually not search the similar patches in the whole image). Then, similar patches are combined to construct a 3-D tensor. Next, the tensor unfolds into a matrix along mode-3, and a weighted low-rank constraint is applied to estimate the abundance matrix of these patches. Finally, the reconstructed abundance matrix of these patches is folded into a tensor so that an estimated abundance image of the local patch is obtained. Meanwhile, collaborative sparsity and TV regularization jointly improve the unmixing performance.

This study makes three contributions.

1) The nonlocal cubic patches are grouped together to form series of low-rank tensors (using weighted nuclear norm) that have potential in exploring the spatial-spectral information deeply and have been proven to perform better than conventional low-rank regularizers in sparse unmixing of HSIs.
2) By utilizing TV, collaborative sparsity and nonlocal tensor low-rank regularizations, the proposed method simultaneously exploits the local spatial smoothness, global row sparsity, and nonlocal low rankness, thus suppressing noises and maintaining the structural information of the abundance image much better.
3) The proposed model can be effectively solved by ADMM algorithm and extensive experimental results validate its superiority in the field of hyperspectral unmixing.

In Section II, we discuss the notations and preliminaries of the tensor and the sparse unmixing of HSI based on the LMM. In Section III, the weighted low-rank tensor decomposition method and the steps for solving the proposed model are described in detail. Section IV analyzes the experimental results for both the simulated and real hyperspectral datasets. Finally, in Section V, we conclude the study.

II. Related Work

A. Tensor Notation and Preliminaries

In this section, we illustrate some notation and preliminaries for the tensors that are used in this article. We use lowercase letters to denote scalars, i.e., t. Vectors are represented by lowercase bold letters, i.e., $\mathbf{t}$. Matrices are denoted by uppercase bold letters, i.e., $\mathbf{T}$. Tensors are represented by uppercase bold calligraphic letters, i.e., $\mathcal{T}$. A tensor can be considered to be a multidimensional number sequence, and its mode number represents

its order [65]. For an M-order tensor $\mathcal{T} \in \mathbb{R}^{I_1 \times I_2 \times \cdots \times I_M}$, the element value of tensor $\mathcal{T}$ at the $(i_1, i_2, \ldots, i_M)$ location is denoted by $t_{i_1,i_2,\ldots,i_M}$, where $i_1 = 1, 2, \ldots, I_1$, $i_2 = 1, 2, \ldots, I_2$, $\cdots$, $i_M = 1, 2, \ldots, I_M$. We give the definitions for a tensor in the following.

Definition 1 (the norm of a tensor): Given an M-order tensor $\mathcal{T} \in \mathbb{R}^{I_1 \times I_2 \times \cdots \times I_M}$, the Frobenius norm of $\mathcal{T}$ is

$$\|\mathcal{T}\|_F = \sqrt{\sum_{i_1=1}^{I_1} \sum_{i_2=2}^{I_2} \cdots \sum_{i_M=1}^{I_M} |t_{i_1,i_2,\ldots,i_M}|^2}. \quad (1)$$

The l_1 norm is calculated as

$$||\mathcal{T}||_1 = \sum_{i_1=1}^{I_1} \sum_{i_2=2}^{I_2} \cdots \sum_{i_M=1}^{I_M} |t_{i_1,i_2,\ldots,i_M}|. \quad (2)$$

Definition 2 (the mode-m unfolding and folding of a tensor): Let $\mathcal{T} \in \mathbb{R}^{I_1 \times I_2 \times \cdots \times I_M}$ be an M-order tensor. The unfolding of $\mathcal{T}$ along mode-m, where $m = I_1, I_2, \ldots, I_M$, can be expressed as $\mathbf{T}_{(m)} \in \mathbb{R}^{I_m \times (I_1 \times I_2 \times \cdots \times I_{m-1} \times I_{m+1} \times \cdots \times I_M)}$. The term fold_m represents the inverse operation of unfolding along mode-m, i.e., $\mathcal{T} = \text{fold}_m(\mathbf{T}_{(m)})$.

Definition 3 (the m-order product of a tensor and a matrix): Given an M-order tensor $\mathcal{T} \in \mathbb{R}^{I_1 \times I_2 \times \cdots \times I_M}$ and a matrix $\mathbf{O} \in \mathbb{R}^{J_m \times I_m}$, the m-order product of $\mathcal{T}$ and $\mathbf{O}$ is defined as

$$\mathcal{Z} = \mathcal{T} \times_m \mathbf{O} \quad (3)$$

where $\mathcal{Z} \in \mathbb{R}^{I_1 \times I_2 \times \cdots \times I_{m-1} \times J_m \times I_{m+1} \times \cdots \times I_M}$.

B. Linear Spectral Unmixing Model

The LMM assumes that an observed HSI $\mathcal{Y} \in \mathbb{R}^{r \times c \times b}$ can be represented as the endmember spectrum in the HSI multiplied by the corresponding abundance coefficient [66], i.e.,

$$\mathcal{Y} = \mathcal{U} \times_3 \mathbf{E} + \mathcal{N} \quad (4)$$

where $\mathbf{E} \in \mathbb{R}^{b \times s}$ is the endmember matrix, $\mathcal{U} \in \mathbb{R}^{r \times c \times s}$ represents the abundance image, $\mathcal{N} \in \mathbb{R}^{r \times c \times b}$ denotes the noise and model error, s is the number of spectra of $\mathbf{E}$, and r, c, and b are the height, width, and number of the spectral bands in the HSI, respectively.

C. Sparse Unmixing Model

Sparse unmixing replaces the endmember matrix with a large spectral library $\mathbf{A} \in \mathbb{R}^{b \times l}$, where l represents the spectrum number contained in $\mathbf{A}$. The sparse unmixing model is

$$\mathcal{Y} = \mathcal{X} \times_3 \mathbf{A} + \mathcal{N} \quad (5)$$

where $\mathcal{X} \in \mathbb{R}^{r \times c \times l}$ represents the abundance image corresponding to $\mathbf{A}$.

Sparse unmixing is based on the fact that the endmember spectrum number in the HSI is much smaller than the spectrum number contained in the spectral library. Thus, there are only a few nonzero values in $\mathcal{X}$, which implies that $\mathcal{X}$ is sparse. Considering the physical meaning, the ANC is used to ensure that there are no negative values in the abundance image. The sparse unmixing optimization problem can be described as

$$\min_{\mathcal{X}} \frac{1}{2}||\mathcal{X} \times_3 \mathbf{A} - \mathcal{Y}||_F^2 + \lambda||\mathcal{X}||_0 \quad \text{s.t. } \mathcal{X} \geq 0 \quad (6)$$

where λ denotes the sparsity parameter and $||\mathcal{X}||_0$ represents the number of nonzero values in $\mathcal{X}$.

Since (6) is a nonconvex optimization problem, it is difficult to solve. However, with the restricted isometry property (RIP) condition [67], (6) can be transformed into a convex optimization problem using the l_1 norm. The optimization problem becomes

$$\min_{\mathcal{X}} \frac{1}{2}||\mathcal{X} \times_3 \mathbf{A} - \mathcal{Y}||_F^2 + \lambda||\mathcal{X}||_1 \quad \text{s.t. } \mathcal{X} \geq 0 \quad (7)$$

where $||\mathcal{X}||_1 = \sum_{i=1}^{r} \sum_{j=1}^{c} \sum_{m=1}^{l} |x_{i,j,m}|$.

The HSI usually contains only a small number of endmembers. Multiplying the corresponding abundance image by a spectral library containing a large number of spectra to represent this HSI inevitably results in an abundance image that contains only a few nonzero values, and all pixels in the abundance image share the same active set of endmembers. That is to say, the abundance image shows sparsity along the spectral dimension. To make use of this prior, the $l_{2,1}$ norm is then enforced on the abundance image $\mathcal{X}$ unfolding along mode-3. The model can be described as

$$\min_{\mathcal{X}} \frac{1}{2}||\mathcal{X} \times_3 \mathbf{A} - \mathcal{Y}||_F^2 + \lambda||\mathcal{X}||_{2,1} \quad \text{s.t. } \mathcal{X} \geq 0 \quad (8)$$

where the collaborative sparsity regularization can be defined as

$$||\mathcal{X}||_{2,1} = ||\mathbf{X}_{(3)}||_{2,1} = \sum_{i=1}^{l} \sqrt{\sum_{j=1}^{r \times c} x_{ij}^2} \quad (9)$$

where $\mathbf{X}_{(3)} \in \mathbb{R}^{l \times (r \times c)}$ and x_{ij} is the element in $\mathbf{X}_{(3)}$.

However, the above-mentioned unmixing method ignores the spatial correlation in the HSI. In order to consider the spatial correlation, an anisotropic TV regularization [45] is added to (7) to promote a smooth transition between adjacent pixels. The problem can be written as

$$\min_{\mathcal{X}} \frac{1}{2}||\mathcal{X} \times_3 \mathbf{A} - \mathcal{Y}||_F^2 + \lambda||\mathcal{X}||_1 + \lambda_{TV}||\mathcal{X}||_{TV} \quad \text{s.t. } \mathcal{X} \geq 0 \quad (10)$$

where λ_{TV} is the parameter of TV regularization. The anisotropic TV can be defined as

$$||\mathcal{X}||_{TV} = ||\mathcal{D}\mathcal{X}||_1 = ||\mathcal{D}_h\mathcal{X}||_1 + ||\mathcal{D}_v\mathcal{X}||_1 \quad (11)$$

where $\mathcal{D}$ is composed of two operators, $\mathcal{D}_h$ and $\mathcal{D}_v$, that calculate the horizontal and vertical differential in the spatial domain, respectively. Let $\mathcal{X}(r_i, c_j, l_k)$ denote the intensity at the location (r_i, c_j, l_k), so the two differential operators can be defined as

$$\begin{cases} \mathcal{D}_h\mathcal{X}(r_i, c_j, l_k) = \mathcal{X}(r_i, c_j + 1, l_k) - \mathcal{X}(r_i, c_j, l_k) \\ \mathcal{D}_v\mathcal{X}(r_i, c_j, l_k) = \mathcal{X}(r_i + 1, c_j, l_k) - \mathcal{X}(r_i, c_j, l_k) \end{cases} \quad (12)$$

where $r_i = 1, 2, \ldots, r$, $c_j = 1, 2, \ldots, c$ and $l_k = 1, 2, \ldots, l$.

Although the methods discussed above have some advantages, they do not use the spatial and spectral information fully. Thus, we propose weighted low-rank tensor decomposition regularization for sparse unmixing (WNLTDSU) of the HSI to further exploit the spatial and spectral information.

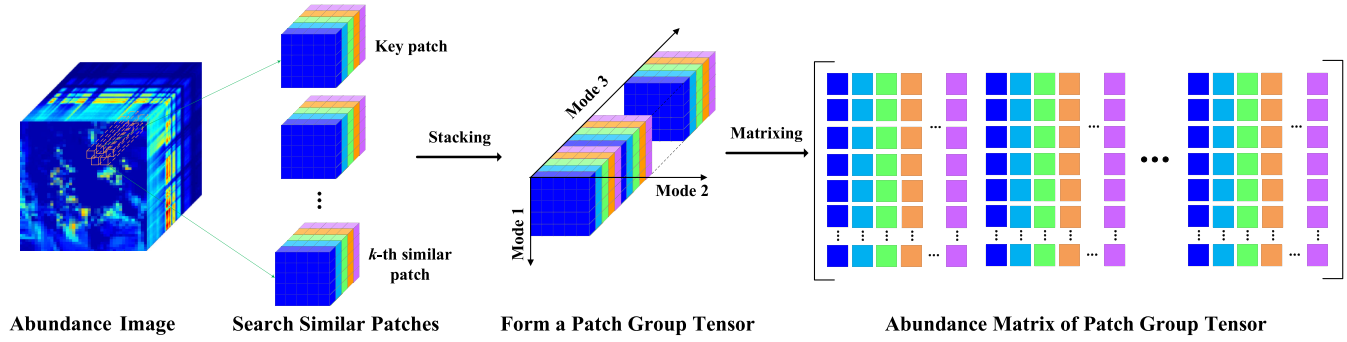

Fig. 2. Procedure for nonlocal low-rank tensor decomposition.

III. Proposed Method

A. Weighted Nonlocal Low-Rank Tensor Decomposition Regularization

The HSI is a 3-D data cube (height, width, and number of spectral bands) that has a high correlation in both the spatial and spectral domains. In the spatial domain, the pixels in a local region have a high correlation, which is reflected in the fact that it contains the same or similar materials. In an HSI, there are many such local regions with similar features. This indicates that HSI has a strong nonlocal similarity. In the abundance image of the HSI, the similarity of the HSI is maintained [68]. Thus, the abundance image can be estimated by the low-rank method. Inspired by this prior, we decided to employ low-rank tensor decomposition to utilize the nonlocal similarity property. The reason is that the HSI is well-suited to representation by tensor due to its 3-D structure, and the tensor representation method maintains the spectral correlation and spatial structure of the HSI at the same time.

The traditional unmixing method vectorizes the abundance image of the HSI according to the spectral dimension and converts it to a 2-D matrix to consider the linear correlation in the spectrum. On this basis, TV regularization is applied to utilize the spatial information. However, considering only the correlation of the spectrum often leads to poor performance, especially in a scene with strong noise, while using only TV to consider the spatial information leads to over-smoothing. To overcome these drawbacks, we propose a weighted low-rank tensor decomposition regularization that associates the spatial and spectral information. Fig. 2 illustrates the procedure for nonlocal low-rank tensor decomposition. Note that the patch group tensor is unfolding along mode-3, and the corresponding abundance matrix is arranged in a square matrix. This is different from the traditional arrangement along the nonlocal similarity mode (mode-2). For example, let the patch size be $5 \times 5 \times 5$. For a key patch, we searched four similar patches in the abundance image, and stacked these patches and the key patch to form a patch group tensor. Then, the tensor was decomposed to the abundance matrix with 25×25 size, while the traditional tensor decomposition methods decomposed the tensor into a 125×5 matrix. The reason we did not adopt the traditional tensor decomposition method is because the abundance image is sparse, and contains many zero values. The unmixing performance using the traditional tensor decomposition is very poor. After several experiments, we found that the best results were obtained by decomposing the tensor into a square abundance matrix.

For the abundance image $\boldsymbol{\mathcal{X}} \in \mathbb{R}^{r \times c \times l}$, we used a local patch, represented by $\boldsymbol{\mathcal{X}}_q \in \mathbb{R}^{r_q \times c_q \times l_q}$, to slide across all dimensions of $\boldsymbol{\mathcal{X}}$, where r, c, and l are, respectively, the height, width, and spectral band number of the abundance image, while r_q, c_q, and l_q are, respectively, the height, width, and spectral band number of the local patch, and $q = 1, 2, \ldots, Q$. The Q represents the total number of patches in the abundance image $\boldsymbol{\mathcal{X}}$. For a local patch $\boldsymbol{\mathcal{X}}_q$, called a key patch, the block matching method [69] was used to search similar patches of $\boldsymbol{\mathcal{X}}_q$ in the abundance image. The k number of patches that are most similar to $\boldsymbol{\mathcal{X}}_q$ and $\boldsymbol{\mathcal{X}}_q$ were stacked to form a patch group tensor, represented by $\boldsymbol{\mathcal{X}}^q \in \mathbb{R}^{r_q \times c_q \times l_q (k+1)}$. Then, the patch group tensor unfolded along mode-3 so that the abundance matrix $\mathbf{X}^q_{(3)}$ of $\boldsymbol{\mathcal{X}}^q$ was obtained. The weighted nuclear norm was used to estimate the abundance matrix of $\boldsymbol{\mathcal{X}}^q$. Hence, we have the following equation:

$$||\boldsymbol{\mathcal{X}}_q||_{w,*} = \sum_{j=1}^{\operatorname{rank}(\mathbf{X}^q_{(3)})} w_j \sigma_j(\mathbf{X}^q_{(3)}) \tag{13}$$

where $\sigma_j(\mathbf{X}^q_{(3)})$ and $w_j \geq 0$ represent the jth singular value and the weight corresponding to the jth singular value in $\mathbf{X}^q_{(3)}$, respectively.

In order to determine the weight w, we took advantage of the fact that the larger singular value in $\mathbf{X}^q_{(3)}$ represents the main components. In the process of unmixing, we try to retain the larger singular value and shrink the smaller singular value. Hence, the weight of the jth singular value w_j should be inversely proportional to the singular value $\sigma_j(\mathbf{X}^q_{(3)})$, which can be defined as

$$w_j = d\sqrt{(k+1)}/(\sigma_j(\mathbf{X}^q_{(3)}) + \delta) \tag{14}$$

where $d > 0$ represents a constant, k is the number of patches that are most similar to $\boldsymbol{\mathcal{X}}_q$, and $\delta = 10^{-16}$ is used to ensure the denominator is not zero.

With the weight setting above, the estimated abundance matrix $\hat{\mathbf{X}}^q_{(3)}$ can be solved using the singular value threshold method:

$$\hat{\mathbf{X}}^q_{(3)} = \mathbf{U}\mathbf{S}_w\left(\sum\right)\mathbf{V}^T \tag{15}$$

where $\mathbf{S}_w(\sum)$ is the soft threshold function under the weight w, and $\mathbf{U}$ and $\mathbf{V}$ are the left singular matrix and right singular matrix, respectively. The estimated abundance image $\hat{\boldsymbol{\mathcal{X}}}^q$ can be obtained by $\text{fold}_3(\hat{\mathbf{X}}^q_{(3)})$.

Applying the above operation to Q local patches, the abundance image $\boldsymbol{\mathcal{X}}$ can be estimated. Thus, the weighted low-rank tensor decomposition regularization can be defined as

$$||\boldsymbol{\mathcal{X}}||_{w,*} = \sum_{q=1}^{Q} ||\boldsymbol{\mathcal{X}}_q||_{w,*} \tag{16}$$

where Q represents the total number of patches in the abundance image $\boldsymbol{\mathcal{X}}$.

B. Proposed Model and Optimization

After adding three regularizations, collaborative sparsity, TV, and weighted nonlocal low-rank tensor decomposition to the sparse unmixing model, the problem of the proposed WNLTDSU method is

$$\begin{aligned}\min_{\boldsymbol{\mathcal{X}}} &\frac{1}{2}||\mathcal{X}\times_3\mathbf{A} - \mathcal{Y}||_F^2 + \lambda||\mathcal{X}||_{2,1} \\ &+ \lambda_{TV}||\mathcal{D}\mathcal{X}||_1 + \lambda_{WT}||\mathcal{X}||_{w,*} \quad \text{s.t. } \mathcal{X} \geq 0\end{aligned} \tag{17}$$

where λ, λ_{TV}, and λ_{WT} represent the contributions of the collaborative sparsity, TV, and weighted nonlocal low-rank tensor decomposition regularizations in the proposed model, respectively.

The proposed model is difficult to solve directly. Therefore, we used the alternating direction method of multipliers (ADMM) [70] to transform the problem of (17) into several subproblems that are easy to solve. With the ADMM, (17) can be equivalently converted to

$$\begin{aligned}\min_{\boldsymbol{\mathcal{X}}} &\frac{1}{2}||\boldsymbol{\mathcal{G}}_1 - \boldsymbol{\mathcal{Y}}||_F^2 + \lambda||\boldsymbol{\mathcal{G}}_2||_{2,1} \\ &+ \lambda_{TV}||\boldsymbol{\mathcal{G}}_4||_1 + \lambda_{WT}||\boldsymbol{\mathcal{G}}_5||_{w,*} + l_{R^+}(\boldsymbol{\mathcal{G}}_6) \\ \text{s.t. } &\boldsymbol{\mathcal{G}}_1 = \boldsymbol{\mathcal{X}}\times_3\mathbf{A} \\ &\boldsymbol{\mathcal{G}}_2 = \boldsymbol{\mathcal{X}} \\ &\boldsymbol{\mathcal{G}}_3 = \boldsymbol{\mathcal{X}} \\ &\boldsymbol{\mathcal{G}}_4 = \mathcal{D}\boldsymbol{\mathcal{G}}_3 \\ &\boldsymbol{\mathcal{G}}_5 = \boldsymbol{\mathcal{X}} \\ &\boldsymbol{\mathcal{G}}_6 = \boldsymbol{\mathcal{X}}\end{aligned} \tag{18}$$

where $\boldsymbol{\mathcal{G}}_1, \boldsymbol{\mathcal{G}}_2, \boldsymbol{\mathcal{G}}_3, \boldsymbol{\mathcal{G}}_4, \boldsymbol{\mathcal{G}}_5$, and $\boldsymbol{\mathcal{G}}_6$ are six introduced variables, which transforms the proposed model into several subproblems. $l_{R^+}(\boldsymbol{\mathcal{X}})$ is used to ensure that the solution to $\boldsymbol{\mathcal{X}}$ is greater than or equal to zero (if $\boldsymbol{\mathcal{X}} \geq 0$, $l_{R^+}(\boldsymbol{\mathcal{X}}) = 0$; otherwise $l_{R^+}(\boldsymbol{\mathcal{X}}) = +\infty$).

The Lagrangian function associated with (18) is

$$\begin{aligned}&\mathcal{L}(\boldsymbol{X}, \boldsymbol{G}_1, \boldsymbol{G}_2, \boldsymbol{G}_3, \boldsymbol{G}_4, \boldsymbol{G}_5, \boldsymbol{G}_6, \boldsymbol{H}_1, \boldsymbol{H}_2, \boldsymbol{H}_3, \boldsymbol{H}_4, \boldsymbol{H}_5, \boldsymbol{H}_6) \\ &= \min_{\boldsymbol{X}} \frac{1}{2}||\boldsymbol{G}_1 - \boldsymbol{Y}||_F^2 + \lambda||\boldsymbol{G}_2||_{2,1} \\ &\quad + \lambda_{TV}||\boldsymbol{G}_4||_1 + \lambda_{WT}||\boldsymbol{G}_5||_{w,*} + l_{R^+}(\boldsymbol{G}_6) \\ &\quad + \frac{\mu}{2}||\boldsymbol{G}_1 - \boldsymbol{X}\times_3\boldsymbol{A} + \boldsymbol{H}_1||_F^2 + \frac{\mu}{2}||\boldsymbol{G}_2 - \boldsymbol{X} + \boldsymbol{H}_2||_F^2 \\ &\quad + \frac{\mu}{2}||\boldsymbol{G}_3 - \boldsymbol{X} + \boldsymbol{H}_3||_F^2 + \frac{\mu}{2}||\boldsymbol{G}_4 - \mathcal{D}\boldsymbol{G}_3 + \boldsymbol{H}_4||_F^2 \\ &\quad + \frac{\mu}{2}||\boldsymbol{G}_5 - \boldsymbol{X} + \boldsymbol{H}_5||_F^2 + \frac{\mu}{2}||\boldsymbol{G}_6 - \boldsymbol{X} + \boldsymbol{H}_6||_F^2\end{aligned} \tag{19}$$

where μ represents the Lagrangian penalty factor, and $\boldsymbol{\mathcal{H}}_1$, $\boldsymbol{\mathcal{H}}_2$, $\boldsymbol{\mathcal{H}}_3$, $\boldsymbol{\mathcal{H}}_4$, $\boldsymbol{\mathcal{H}}_5$, and $\boldsymbol{\mathcal{H}}_6$ denote the six Lagrangian multipliers.

According to the ADMM, the $\boldsymbol{\mathcal{X}}, \boldsymbol{\mathcal{G}}_1, \boldsymbol{\mathcal{G}}_2, \boldsymbol{\mathcal{G}}_3, \boldsymbol{\mathcal{G}}_4, \boldsymbol{\mathcal{G}}_5$, and $\boldsymbol{\mathcal{G}}_6$ are solved iteratively in sequence. In the following, we discuss the solutions to these subproblems. The optimization problem of $\boldsymbol{\mathcal{X}}$ is

$$\begin{aligned}\boldsymbol{\mathcal{X}}^{[i+1]} = \arg\min_{\boldsymbol{\mathcal{X}}} &\frac{\mu}{2}||\boldsymbol{\mathcal{G}}_1^{[i]} - \boldsymbol{\mathcal{X}}\times_3\mathbf{A} + \boldsymbol{\mathcal{H}}_1^{[i]}||_F^2 \\ &+ \frac{\mu}{2}||\boldsymbol{\mathcal{G}}_2^{[i]} - \boldsymbol{\mathcal{X}} + \boldsymbol{\mathcal{H}}_2^{[i]}||_F^2 + \frac{\mu}{2}||\boldsymbol{\mathcal{G}}_3^{[i]} - \boldsymbol{\mathcal{X}} + \boldsymbol{\mathcal{H}}_3^{[i]}||_F^2 \\ &+ \frac{\mu}{2}||\boldsymbol{\mathcal{G}}_5^{[i]} - \boldsymbol{\mathcal{X}} + \boldsymbol{\mathcal{H}}_5^{[i]}||_F^2 + \frac{\mu}{2}||\boldsymbol{\mathcal{G}}_6^{[i]} - \boldsymbol{\mathcal{X}} + \boldsymbol{\mathcal{H}}_6^{[i]}||_F^2.\end{aligned} \tag{20}$$

The solution to (20) is

$$\begin{aligned}\boldsymbol{\mathcal{X}}^{[i+1]} = &((\boldsymbol{\mathcal{G}}_1^{[i]} + \boldsymbol{\mathcal{H}}_1^{[i]})\times_3\mathbf{A}^T + \boldsymbol{\mathcal{G}}_2^{[i]} + \boldsymbol{\mathcal{H}}_2^{[i]} + \boldsymbol{\mathcal{G}}_3^{[i]} \\ &+ \boldsymbol{\mathcal{H}}_3^{[i]} + \boldsymbol{\mathcal{G}}_5^{[i]} + \boldsymbol{\mathcal{H}}_5^{[i]} + \boldsymbol{\mathcal{G}}_6^{[i]} + \boldsymbol{\mathcal{H}}_6^{[i]})\times_3(\mathbf{A}^T\mathbf{A} + 4\mathbf{I})^{-1}\end{aligned} \tag{21}$$

where $\mathbf{I}$ represents the identity matrix, and $\mathbf{A}^T$ denotes the transpose of $\mathbf{A}$.

The optimization problem of $\boldsymbol{\mathcal{G}}_1, \boldsymbol{\mathcal{G}}_2, \boldsymbol{\mathcal{G}}_3, \boldsymbol{\mathcal{G}}_4, \boldsymbol{\mathcal{G}}_5$, and $\boldsymbol{\mathcal{G}}_6$ can be expressed as follows:

$$\begin{aligned}\boldsymbol{\mathcal{G}}_1^{[i+1]} = \arg\min_{\boldsymbol{\mathcal{G}}_1} &\frac{1}{2}||\boldsymbol{\mathcal{G}}_1 - \boldsymbol{\mathcal{Y}}||_F^2 + \frac{\mu}{2}||\boldsymbol{\mathcal{G}}_1 \\ &- \boldsymbol{\mathcal{X}}^{[i]}\times_3\mathbf{A} + \boldsymbol{\mathcal{H}}_1^{[i]}||_F^2.\end{aligned} \tag{22}$$

$$\boldsymbol{\mathcal{G}}_2^{[i+1]} = \arg\min_{\boldsymbol{\mathcal{G}}_2} \lambda||\boldsymbol{\mathcal{G}}_2||_{2,1} + \frac{\mu}{2}||\boldsymbol{\mathcal{G}}_2 - \boldsymbol{\mathcal{X}}^{[i]} + \boldsymbol{\mathcal{H}}_2^{[i]}||_F^2. \tag{23}$$

$$\begin{aligned}\boldsymbol{\mathcal{G}}_3^{[i+1]} = \arg\min_{\boldsymbol{\mathcal{G}}_3} &\frac{\mu}{2}||\boldsymbol{\mathcal{G}}_3 - \boldsymbol{\mathcal{X}}^{[i]} + \boldsymbol{\mathcal{H}}_3^{[i]}||_F^2 + \frac{\mu}{2}||\boldsymbol{\mathcal{G}}_4^{[i]} \\ &- \mathcal{D}\boldsymbol{\mathcal{G}}_3 + \boldsymbol{\mathcal{H}}_4^{[i]}||_F^2.\end{aligned} \tag{24}$$

$$\boldsymbol{\mathcal{G}}_4^{[i+1]} = \arg\min_{\boldsymbol{\mathcal{G}}_4} \lambda_{TV}||\boldsymbol{\mathcal{G}}_4||_1 + \frac{\mu}{2}||\boldsymbol{\mathcal{G}}_4 - \boldsymbol{\mathcal{X}}^{[i]} + \boldsymbol{\mathcal{H}}_4^{[i]}||_F^2. \tag{25}$$

$$\boldsymbol{\mathcal{G}}_5^{[i+1]} = \arg\min_{\boldsymbol{\mathcal{G}}_5} \lambda_{WT}||\boldsymbol{\mathcal{G}}_5||_{w,*} + \frac{\mu}{2}||\boldsymbol{\mathcal{G}}_5 - \boldsymbol{\mathcal{X}}^{[i]} + \boldsymbol{\mathcal{H}}_5^{[i]}||_F^2. \tag{26}$$

$$\boldsymbol{\mathcal{G}}_6^{[i+1]} = \arg\min_{\boldsymbol{\mathcal{G}}_6} l_{R^+}(\boldsymbol{\mathcal{G}}_6) + \frac{\mu}{2}||\boldsymbol{\mathcal{G}}_6 - \boldsymbol{\mathcal{X}}^{[i]} + \boldsymbol{\mathcal{H}}_6^{[i]}||_F^2. \tag{27}$$

The solution to $\boldsymbol{\mathcal{G}}_1$ is

$$\boldsymbol{\mathcal{G}}_1^{[i+1]} = \frac{1}{1+\mu}[\boldsymbol{\mathcal{Y}} + \mu(\boldsymbol{\mathcal{X}}^{[i]}\times_3\mathbf{A} - \boldsymbol{\mathcal{H}}_1^{[i]}||_F^2)]. \tag{28}$$

For collaborative sparsity regularization, the solution is obtained by the vect-soft threshold [71]

$$\boldsymbol{\mathcal{G}}_2^{[i+1]} = \text{vect} - \text{soft}\left(\boldsymbol{\mathcal{X}}^{[i]} - \boldsymbol{\mathcal{H}}_2^{[i]}, \frac{\lambda}{\mu}\right) \tag{29}$$

where the vect-soft-threshold function is calculated as $\text{vect}-\text{soft}(\varphi,\zeta)=\varphi(\max\{||\varphi||_2-\zeta,0\}/\max\{||\varphi||_2-\zeta,0\}+\zeta)$.

$\boldsymbol{\mathcal{G}}_3$ can be calculated by

$$\left(\mathcal{D}^T\mathcal{D}+\boldsymbol{\mathcal{I}}\right)\boldsymbol{\mathcal{G}}_3^{[i+1]}=\left(\boldsymbol{\mathcal{X}}^{[i]}-\boldsymbol{\mathcal{H}}_3^{[i]}+\mathcal{D}^T(\boldsymbol{\mathcal{G}}_4^{[i]}+\boldsymbol{\mathcal{H}}_4^{[i]})\right) \tag{30}$$

where $\boldsymbol{\mathcal{I}}$ denotes the identity tensor. $\mathcal{D}$ is a convolution, operating only in the spatial domain. The solution to $\boldsymbol{\mathcal{G}}_3$ in (30) can be acquired by a fast Fourier transform [72]:

$$\boldsymbol{\mathcal{G}}_3^{[i+1]}=ifft\left(\frac{\boldsymbol{\mathcal{X}}^{[i]}-\boldsymbol{\mathcal{H}}_3^{[i]}+\mathcal{D}^T(\boldsymbol{\mathcal{G}}_4^{[i]}+\boldsymbol{\mathcal{H}}_4^{[i]})}{\mathbf{1}+fft(\mathcal{D}_h)^T fft(\mathcal{D}_h)+fft(\mathcal{D}_v)^T fft(\mathcal{D}_v)}\right) \tag{31}$$

where *fft* and *ifft* represent the Fourier transform and the inverse Fourier transform, respectively.

$\boldsymbol{\mathcal{G}}_4$ in TV regularization is solved by the soft threshold [73]:

$$\boldsymbol{\mathcal{G}}_4^{[i+1]}=\text{soft}\left(\boldsymbol{\mathcal{H}}_4^{[i]}-\mathcal{D}\boldsymbol{\mathcal{G}}_3^{[i]},\frac{\lambda_{TV}}{\mu}\right) \tag{32}$$

where $\text{soft}(\varphi,\zeta)$ represents the soft threshold function, and the solution is $\text{soft}(\varphi,\zeta)=\text{sign}(\varphi)\max\{|\varphi|-\zeta,0\}$.

To solve $\boldsymbol{\mathcal{G}}_5$, the weighted nuclear norm is applied to each abundance image of the patch group tensor to obtain the reconstructed abundance image, which can be represented as

$$\boldsymbol{\mathcal{G}}_5^{[i+1]}=\text{shrinkage}\left(\boldsymbol{\mathcal{X}}^{[i]}-\boldsymbol{\mathcal{H}}_5^{[i]},\frac{w\lambda_{WT}}{\mu}\right) \tag{33}$$

where $\text{shrinkage}(\varphi,\zeta)=\text{diag}(\max\{SVD(\varphi)-\zeta,0\})$, $SVD(\cdot)$ denotes singular value decomposition.

Finally, the solution to $\boldsymbol{\mathcal{G}}_6$ is solved by

$$\boldsymbol{\mathcal{G}}_6^{[i+1]}=\max\left(\boldsymbol{\mathcal{X}}^{[i]}-\boldsymbol{\mathcal{H}}_6^{[i]},0\right). \tag{34}$$

In each iteration, $\boldsymbol{\mathcal{X}}$ is first updated, and then $\boldsymbol{\mathcal{G}}_1$, $\boldsymbol{\mathcal{G}}_2$, $\boldsymbol{\mathcal{G}}_3$, $\boldsymbol{\mathcal{G}}_4$, $\boldsymbol{\mathcal{G}}_5$, and $\boldsymbol{\mathcal{G}}_6$ are updated in sequence. When the stop condition is satisfied, the model stops iterating and outputs the abundance image $\boldsymbol{\mathcal{X}}$. The pseudocode for the proposed model is given in Algorithm 1.

Algorithm 1: Pseudocode of the Proposed Model.

1. **Initialization**: set $i=0$, choose λ, λ_{TV}, λ_{WT}, μ, $\boldsymbol{\mathcal{X}}^{[0]}$, $\boldsymbol{\mathcal{G}}_1^{[0]},\cdots,\boldsymbol{\mathcal{G}}_6^{[0]}$, $\boldsymbol{\mathcal{H}}_1^{[0]},\cdots,\boldsymbol{\mathcal{H}}_6^{[0]}$
2. **while** some stopping criterion is not satisfied **do**
3. $\mathcal{X}^{[i+1]}=\arg\min_{\boldsymbol{\mathcal{X}}}\mathcal{L}(\mathcal{X},\mathcal{G}_1^{[i]},\ldots,\mathcal{G}_6^{[i]},\mathcal{H}_1^{[i]},\ldots,\mathcal{H}_6^{[i]})$
4. **for** $j=1,\ldots,6$ **do**
5. $\mathcal{G}_j^{[i+1]}=\arg\min_{\mathcal{G}_j}\mathcal{L}(\mathcal{X}^{[i]},\mathcal{G}_1^{[i]},\ldots,\mathcal{G}_j,\ldots,\mathcal{G}_6^{[i]})$
6. **end for**
7. **Update Lagrange multipliers**
8. $\boldsymbol{\mathcal{H}}_1^{[i+1]}=\boldsymbol{\mathcal{H}}_1^{[i]}-\boldsymbol{\mathcal{X}}^{[i+1]}\times_3\mathbf{A}+\boldsymbol{\mathcal{G}}_1^{[i+1]}$
9. $\boldsymbol{\mathcal{H}}_4^{[i+1]}=\boldsymbol{\mathcal{H}}_4^{[i]}-\mathcal{D}\boldsymbol{\mathcal{G}}_3^{[i+1]}+\boldsymbol{\mathcal{G}}_4^{[i+1]}$
10. $\boldsymbol{\mathcal{H}}_j^{[i+1]}=\boldsymbol{\mathcal{H}}_j^{[i]}-\boldsymbol{\mathcal{X}}^{[i+1]}+\boldsymbol{\mathcal{G}}_j^{[i+1]},\ j=2,3,5,6$
11. **Update iteration** $i=i+1$
12. **end while**

C. Computational Efficiency

Before the time complexity discussion, recall that r_q, c_q, and l_q are, respectively, the height, width, and spectral band number of the local patch, k is the number of patches that are most similar to $\boldsymbol{\mathcal{X}}_q$, and Q represents the total number of local patches in the abundance image $\boldsymbol{\mathcal{X}}$. The most time-consuming step of the proposed model is the calculation of $\boldsymbol{\mathcal{G}}_5$. For a patch group tensor, the time complexity of the weighted nonlocal low-rank tensor decomposition step is $O(r_qc_q(l_q(k+1))^2)$. The size of the patch and the number of similar patches affect the complexity of this step. Because there are Q local patches in the abundance image, the overall time-consumption is $O(r_qc_q(l_q(k+1))^2Q)$.

IV. Experiments and Analysis

In this section, we present the unmixing performance of the proposed method (WLTDSU) by utilizing two simulated hyperspectral datasets and one real hyperspectral dataset. We compare the unmixing performance of the proposed method with the performance of several state-of-the-art methods, such as the CLSUnSAL method [40], SUnSAL with TV regularization (SUnSAL-TV) method [45], joint local abundance sparse unmixing (J-LASU) method [60], sparse unmixing with l_1-l_2 sparsity and TV regularization (l_1-l_2 SUnSAL-TV) method [74], and the sparse unmixing with nonlocal low-rank prior (NLLRSU) method [75].

A. Experiments With Simulated Datasets

To construct spectral library $\mathbf{A}$ for the simulated dataset experiments, we used the USGS spectral library (named splib06) [76], which was released in September 2007. Spectral library $\mathbf{A}$ contains 240 spectral curves of different ground objects randomly selected from the splib06. The spectral curves in $\mathbf{A}$ have 224 spectral bands, and the distribution of the spectral curve is between 400–2500 nm. The spectral angle was set to greater than 4.4 to avoid the effect of high mutual coherence between spectral curves in the spectral library.

1) Simulated Dataset 1 (DS1): Five spectral curves were randomly selected from spectral library $\mathbf{A}$ as endmembers to generate the DS1. The data generation followed the LMM and imposed the ANC and sum-to-one constraint on the abundance image, which had 75×75 pixels. As shown in Fig. 3(a), the endmembers are evenly distributed in the square regions. The true abundance images of DS1 are shown in Fig. 3(b)–(f). There are pure regions, denoted in red, composed of pure endmembers, and mixed regions composed of endmembers ranging from two to five. The background pixels are composed of the same five endmembers, but the abundance values of these endmembers are randomly fixed to 0.1149, 0.0741, 0.2003, 0.2055, and 0.4051.

2) Simulated Dataset 2 (DS2): The DS2 had 100×100 pixels and was constructed by randomly selecting nine spectral curves from spectral library $\mathbf{A}$. The distribution of the nine endmembers were constrained by the ANC and sum-to-one constraint. The abundance images of DS2 satisfied the Dirichlet function on the probability simplex. Fig. 4 shows the true

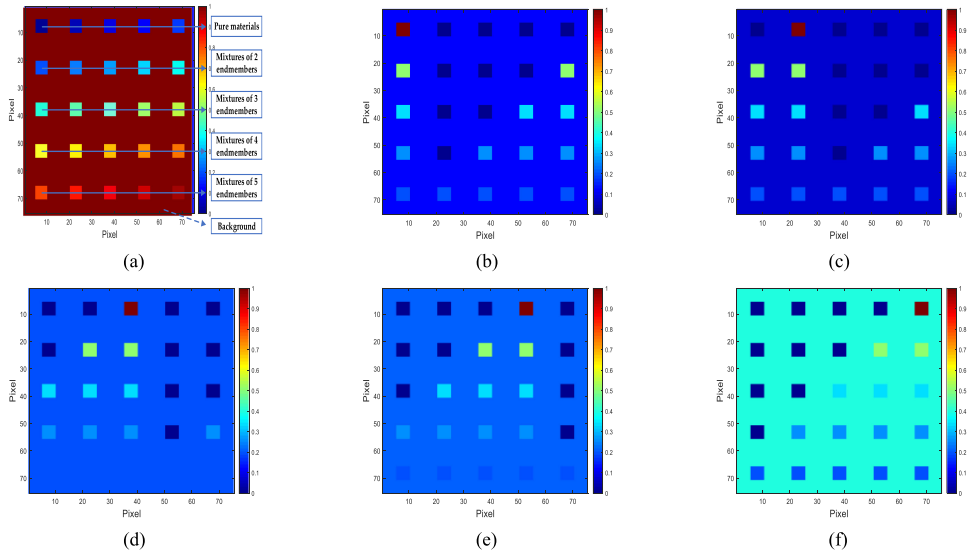

Fig. 3. True abundance images of endmembers in the simulated dataset 1 (DS1). (a) Simulated image. (b) Endmember 1. (c) Endmember 2. (d) Endmember 3. (e) Endmember 4. (f) Endmember 5.

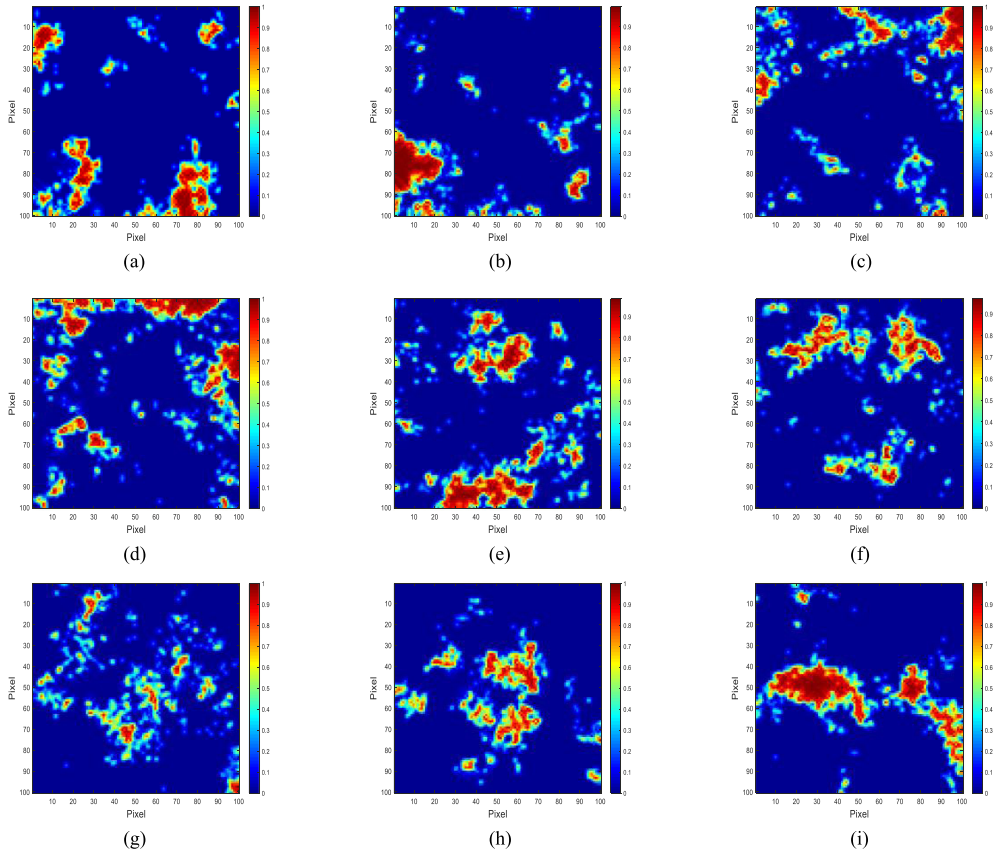

Fig. 4. True fractional abundances of endmembers in the simulated dataset 2 (DS2). (a) Endmember 1. (b) Endmember 2. (c) Endmember 3. (d) Endmember 4. (e) Endmember 5. (f) Endmember 6. (g) Endmember 7. (h) Endmember 8. (i) Endmember 9.

abundance images. The abundance images show homogeneity and piecewise smoothing in the spatial domain.

After DS1 and DS2 were generated, Gaussian noise with three different signal-to-noise ratios (SNRs), i.e., 10, 15, and 20 dB were used to distort these two datasets.

In order to evaluate the performance of the CLSUnSAL, SUnSAL-TV, J-LASU, l_1-l_2 SUnSAL-TV, NLLRSU, and proposed WNLTDSU methods qualitatively, the signal to reconstruction error (SRE) and root mean square error (RMSE) were used in the experiments, and are respectively

TABLE I
PARAMETER SETTINGS

Data		DS1			DS2		
SNR		10 dB	15 dB	20 dB	10 dB	15 dB	20 dB
CLSUnSAL [40]	λ	1×10^{1}	1×10^{1}	8×10^{0}	1×10^{1}	1×10^{1}	3×10^{0}
	μ	5×10^{-2}	1×10^{-1}	1×10^{-1}	5×10^{-2}	5×10^{-2}	1×10^{-1}
SUnSAL-TV [45]	λ	1×10^{-1}	1×10^{-1}	5×10^{-2}	1×10^{-1}	1×10^{-1}	5×10^{-2}
	λ_{TV}	5×10^{-1}	1×10^{-1}	5×10^{-2}	1×10^{-1}	5×10^{-2}	1×10^{-2}
	μ	1×10^{-1}	5×10^{-1}	1×10^{-1}	1×10^{-1}	5×10^{-1}	5×10^{-2}
J-LASU [60]	λ	2×10^{0}	1×10^{0}	2.5×10^{-1}	1×10^{-4}	1×10^{-4}	1×10^{-4}
	λ_{TV}	1×10^{-1}	1×10^{-1}	5×10^{-2}	5×10^{-2}	5×10^{-2}	1×10^{-2}
	λ_{LR}	1×10^{0}	5×10^{-1}	3×10^{-1}	5×10^{-1}	1×10^{-1}	1×10^{-1}
	μ	5×10^{0}	2×10^{0}	1×10^{0}	5×10^{-2}	1×10^{-1}	5×10^{-2}
l_1-l_2 SUnSAL-TV [74]	λ	1×10^{-2}	1×10^{-1}	1×10^{-2}	1×10^{-1}	1×10^{-2}	1×10^{-2}
	λ_{TV}	5×10^{-1}	5×10^{-2}	5×10^{-2}	1×10^{-1}	5×10^{-2}	5×10^{-2}
	μ	1×10^{0}	1×10^{0}	3×10^{-1}	1×10^{0}	5×10^{-1}	1×10^{-1}
NLLRSU [75]	λ	5×10^{-1}	1×10^{-1}	1×10^{-1}	1×10^{-4}	1×10^{-4}	1×10^{-4}
	λ_{TV}	1×10^{-1}	1×10^{-1}	5×10^{-2}	1×10^{-1}	5×10^{-2}	1×10^{-2}
	λ_{NL}	2×10^{0}	5×10^{-1}	5×10^{-1}	1×10^{-0}	5×10^{-1}	1×10^{-1}
	μ	5×10^{0}	1×10^{0}	1×10^{0}	5×10^{-1}	5×10^{-1}	5×10^{-2}
Our Method	λ	5×10^{-2}	5×10^{-3}	1×10^{-3}	5×10^{-4}	5×10^{-4}	1×10^{-4}
	λ_{TV}	1×10^{-1}	5×10^{-2}	5×10^{-3}	1×10^{-1}	5×10^{-2}	1×10^{-2}
	λ_{WT}	2.5×10^{-2}	5×10^{-3}	2.5×10^{-3}	2.5×10^{-2}	5×10^{-3}	5×10^{-4}
	μ	5×10^{-1}	5×10^{-1}	5×10^{-1}	5×10^{-1}	5×10^{-1}	1×10^{-1}

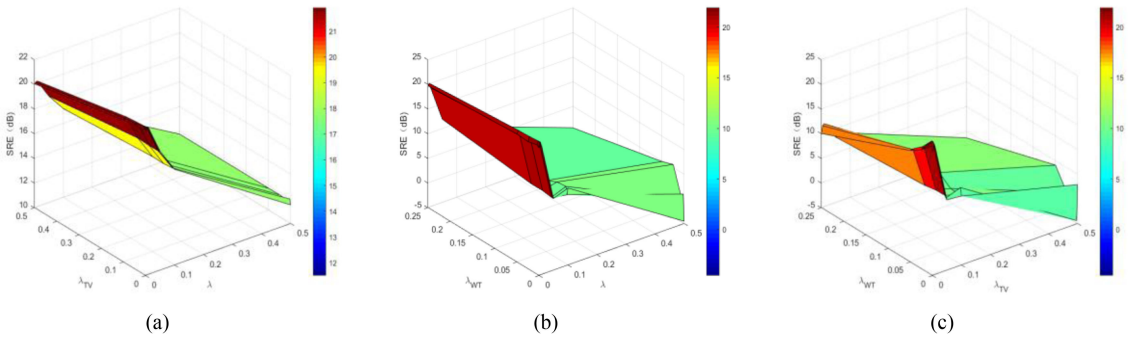

(a) (b) (c)

Fig. 5. SRE (dB) as a function of parameters λ, λ_{TV}, and λ_{WT} for DS1 with a 20 dB SNR level. (**a**) λ and λ_{TV}. (**b**) λ and λ_{WT}. (**c**) λ_{TV} and λ_{WT}.

defined as:

$$\mathrm{SRE(dB)} = \frac{\mathbb{E}[||\boldsymbol{\mathcal{X}}||_2^2]}{\mathbb{E}[||\boldsymbol{\mathcal{X}} - \bar{\boldsymbol{\mathcal{X}}}||_2^2]} \tag{35}$$

$$\mathrm{RMSE} = \sqrt{\frac{1}{r \times c \times l} \sum_{i=1}^{r} \sum_{j=1}^{c} \sum_{k=1}^{l} \left(x_{i,j,k} - \bar{x}_{i,j,k}\right)^2} \tag{36}$$

where $\boldsymbol{\mathcal{X}}$ represents the true abundance image and $x_{i,j,k}$ is the element in $\boldsymbol{\mathcal{X}}$, $\bar{\boldsymbol{\mathcal{X}}}$ denotes the reconstructed abundance image, and $\bar{x}_{i,j,k}$ is the element in $\bar{\boldsymbol{\mathcal{X}}}$. A high SRE value and low RMSE value mean that the unmixing method shows good performance.

Table I shows the parameter settings of the six methods, CLSUnSAL, SUnSAL-TV, J-LASU, l_1-l_2 SUnSAL-TV, NLLRSU, and WNLTDSU, utilized on DS1 and DS2. The parameter for sparsity regularization for the six methods is denoted by λ. The λ_{TV} represents the parameter for TV regularization for the SUnSAL-TV, J-LASU, l_1-l_2 SUnSAL-TV, NLLRSU, and WNLTDSU methods. The local low-rank regularization parameter is λ_{LA} for J-LASU, and the nonlocal low-rank regularization parameter is λ_{NL} for NLLRSU. For WNLTDSU, λ_{WT} represents the parameter of the weighted nonlocal low-rank tensor decomposition regularization. The parameter μ is the Lagrangian penalty factor for the six methods. The values of all the parameters for each method are adjusted optimally.

Fig. 5 presents the SRE (dB) as a function with respect to λ, λ_{TV}, and λ_{WT} under the condition of 20 dB SNR noise in DS1. Because the SRE and three parameters are difficult to display in a figure, we take into account the impact of λ, and λ_{TV}, λ and λ_{WT}, λ_{TV} and λ_{WT} on the SRE results in sequence. It is evident that the change in parameters has a great influence on the SRE

TABLE II
SRE (dB) RESULTS (THE OPTIMAL RESULTS ARE SHOWN IN BOLD TYPE)

Data	SNR	CLSUnSAL [40]	SUnSAL-TV [45]	J-LASU [60]	l_1-l_2 SUnSAL-TV [74]	NLLRSU [75]	Our Method
DS1	10 dB	1.6544	3.9803	10.6039	4.1424	11.5466	**15.7918**
	15 dB	4.4945	6.4204	13.4001	6.0267	13.9307	**18.7277**
	20 dB	6.0518	7.1069	15.3860	7.0245	16.2008	**21.9161**
DS2	10 dB	1.0144	3.6093	3.5925	3.6494	3.9300	**6.0729**
	15 dB	2.3747	4.5860	4.8039	4.8445	5.1034	**7.4840**
	20 dB	3.3961	5.5352	6.3062	6.2078	6.7188	**9.3762**

TABLE III
RMSE RESULTS (THE OPTIMAL RESULTS ARE SHOWN IN BOLD TYPE)

Data	SNR	CLSUnSAL [40]	SUnSAL-TV [45]	J-LASU [60]	l_1-l_2 SUnSAL-TV [74]	NLLRSU [75]	Our Method
DS1	10 dB	0.0286	0.0218	0.0102	0.0214	0.0091	**0.0056**
	15 dB	0.0206	0.0165	0.0074	0.0173	0.0069	**0.0040**
	20 dB	0.0172	0.0152	0.0059	0.0154	0.0053	**0.0028**
DS2	10 dB	0.0438	0.0325	0.0325	0.0323	0.0313	**0.0245**
	15 dB	0.0374	0.0290	0.0283	0.0282	0.0273	**0.0208**
	20 dB	0.0333	0.0260	0.0238	0.0241	0.0227	**0.0167**

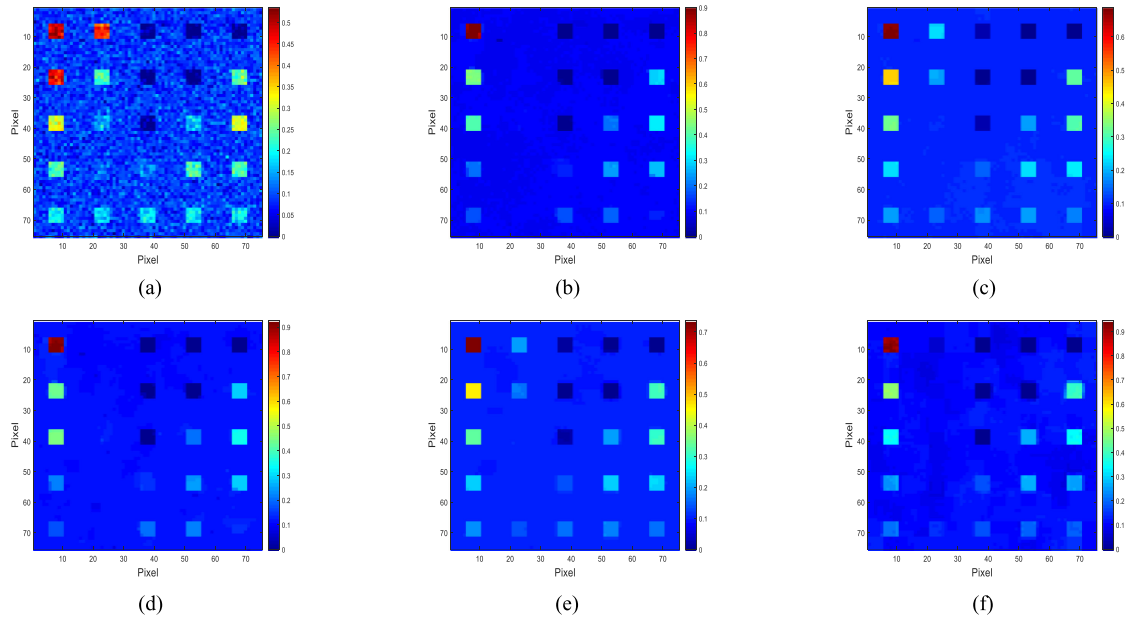

Fig. 6. Estimated fractional abundances of endmember 1 in DS1 with a 20 dB SNR level. (a) CLSUnSAL. (b) SUnSAL-TV. (c) J-LASU; (d) l_1-l_2 SUnSAL-TV. (e) NLLRSU. (f) Our method.

results. In general, the smaller the parameter values, the higher the SRE results, which means better unmixing performance.

Tables II and III show the SRE and RMSE results for DS1 and DS2 unmixed by the six methods, respectively. From these tables, it can be seen that those methods considering both spectral correlation and the spatial information, such as SUnSAL-TV, J-LASU, l_1-l_2 SUnSAL-TV, NLLRSU, and our method, perform better than the CLSUnSAL method which only considers the spectral correlation. In addition, the results obtained by our method are best. For example, in the case of DS1 with 20dB SNR, the SRE result obtained by our method is 5.72dB higher than NLLRSU, while the RMSE result is 0.0025 lower than NLLRSU. Figs. 6–9 present abundance images estimated by the six methods at the 20 dB SNR noise level. Here, we present only the abundance images of the two randomly selected endmembers from DS1, and two endmembers from DS2, because the other endmembers show similar unmixing results. From these figures, it can be observed that the abundance image estimated by CLSUnSAL is greatly affected by noise, while the SUnSAL-TV method shows the smoothest unmixing results of the six methods. Compared with the CLSUnSAL, SUnSAL-TV, l_1-l_2 SUnSAL-TV methods, the J-LASU, NLLRSU, and our method take into account the low-rank property of abundant images so that they can better maintain the structure information of the maps. Compared with these five methods, the abundance images reconstructed by our method better maintain the structure

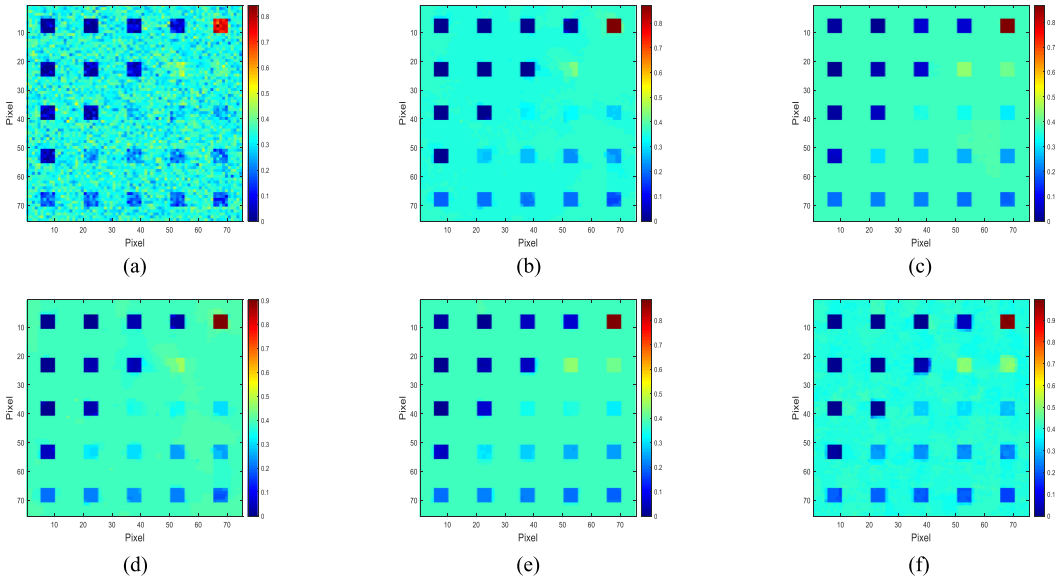

Fig. 7. Estimated fractional abundances of endmember 5 in DS1 with a 20 dB SNR level. (a) CLSUnSAL. (b) SUnSAL-TV. (c) J-LASU. (d) l_1-l_2 SUnSAL-TV. (e) NLLRSU. (f) Our method.

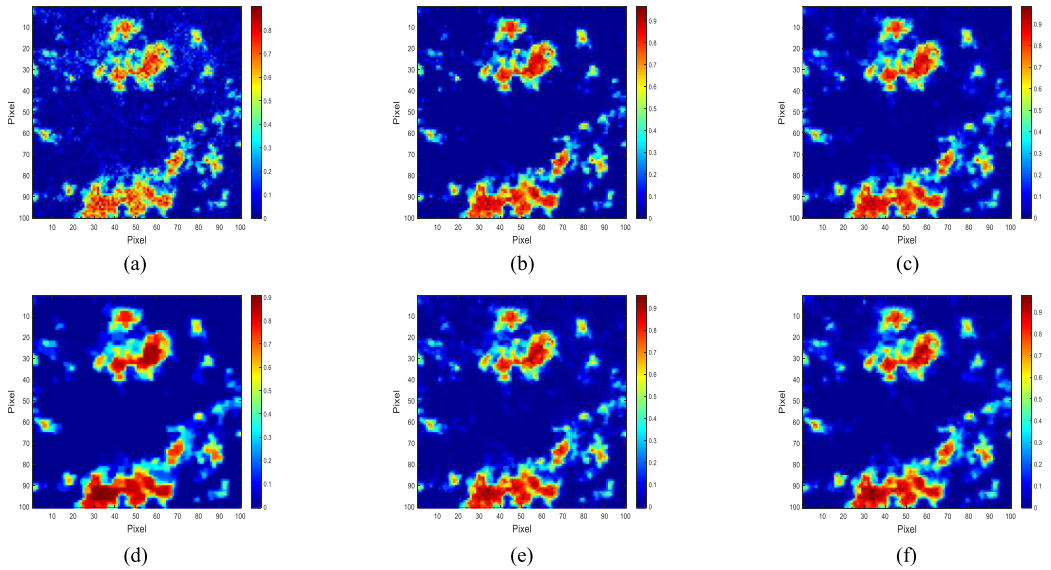

Fig. 8. Estimated fractional abundances of endmember 5 in DS2 with a 20 dB SNR level. (a) CLSUnSAL. (b) SUnSAL-TV. (c) J-LASU. (d) l_1-l_2 SUnSAL-TV. (e) NLLRSU. (f) Our method.

information, for example, the image estimated by our method is closer to the ground truth in the edge transition region. In a word, the proposed method is not only better at noise suppression but is also closest to the real abundance images among the six methods.

B. Experiments With Real Datasets

In this experiment, the well-known AVIRIS Cuprite mineral map dataset was used for real hyperspectral data experiments. The dataset contains 224 spectral bands ranging from 400 to 2500 nm. Fig. 10 shows the mine distribution for this dataset. The 50 spectral signatures are chosen from USGS library for unmixing the Cuprite mineral map dataset. A subset of this dataset, containing 250 $\times$ 191 pixels, was used in the experiment. The bands 1, 2, 105–115, 150–170, 223, and 224 were removed because of the strong noise and water absorption effects. Thus, the subset contained 188 bands.

Fig. 11 presents the abundance images estimated by the six unmixing methods. Three kinds of abundance images for minerals, Alunite, Buddingtonite, and Chalcedony, are shown from left to right, respectively. The first row is the actual distribution of the three minerals and is treated as ground truth. It is important to note that the actual distributions of the three minerals were generated by Tricorder 3.3 software in 1995, while the dataset used in the experiments was released in 1997, so we used the mineral map only for visual qualitative analysis. The next few rows are the unmixing results obtained by CLSUnSAL, SUnSAL-TV,

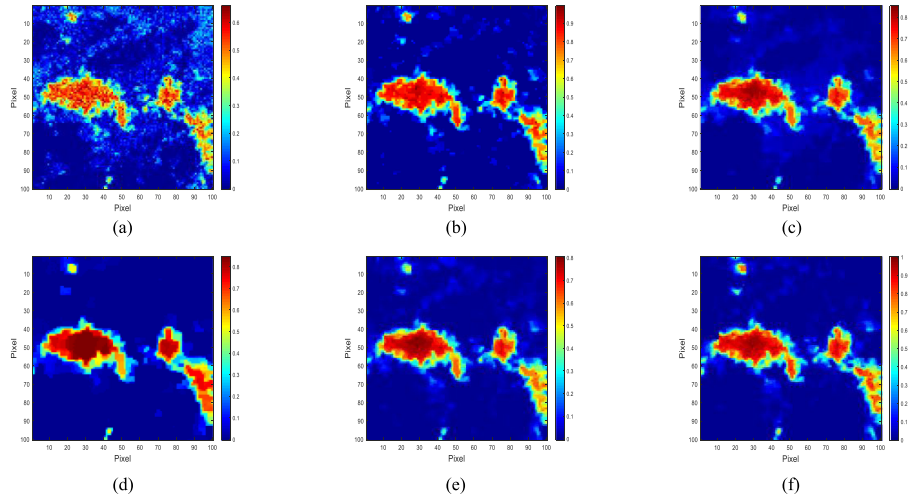

Fig. 9. Estimated fractional abundances of endmember 9 in DS2 with a 20 dB SNR level. (a) CLSUnSAL. (b) SUnSAL-TV. (c) J-LASU. (d) l_1-l_2 SUnSAL-TV. (e) NLLRSU. (f) Our method.

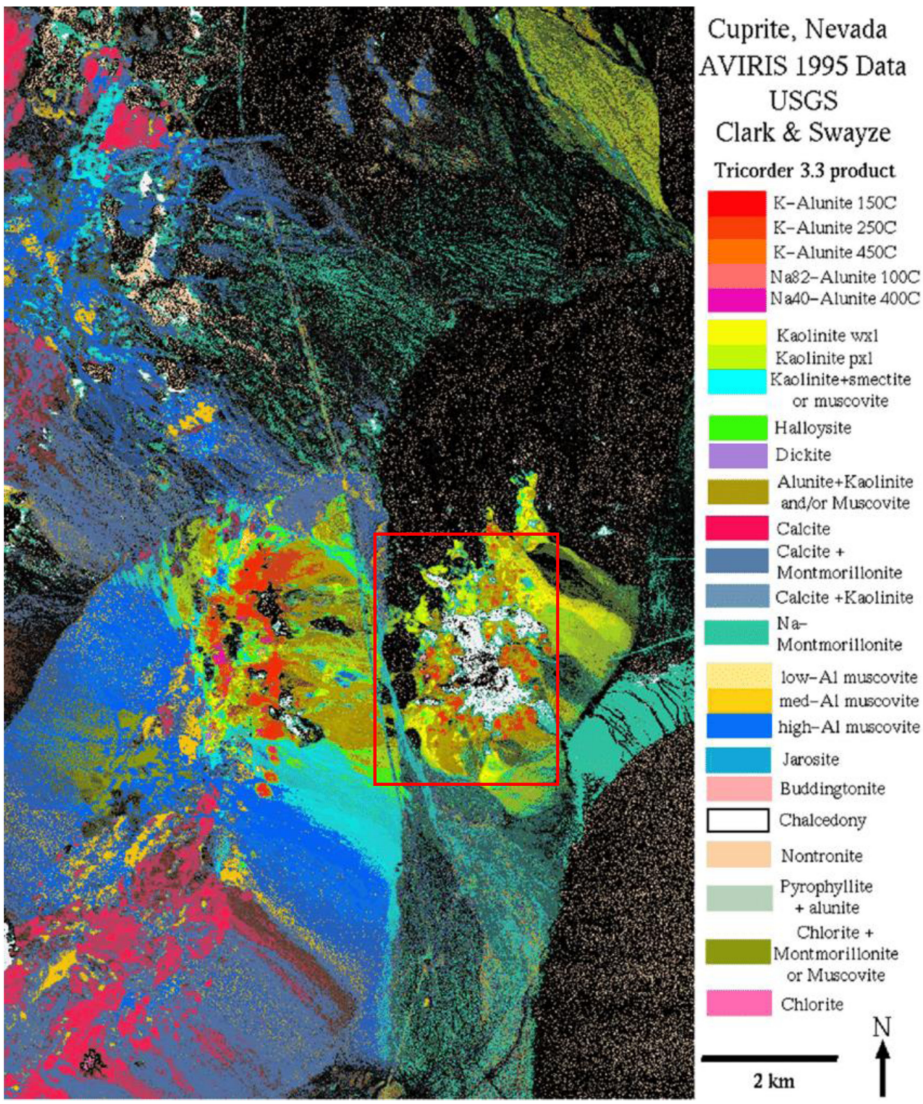

Fig. 10. USGS mineral map of Cuprite in Nevada. The area shown in red rectangle is the dataset used in the experiment.

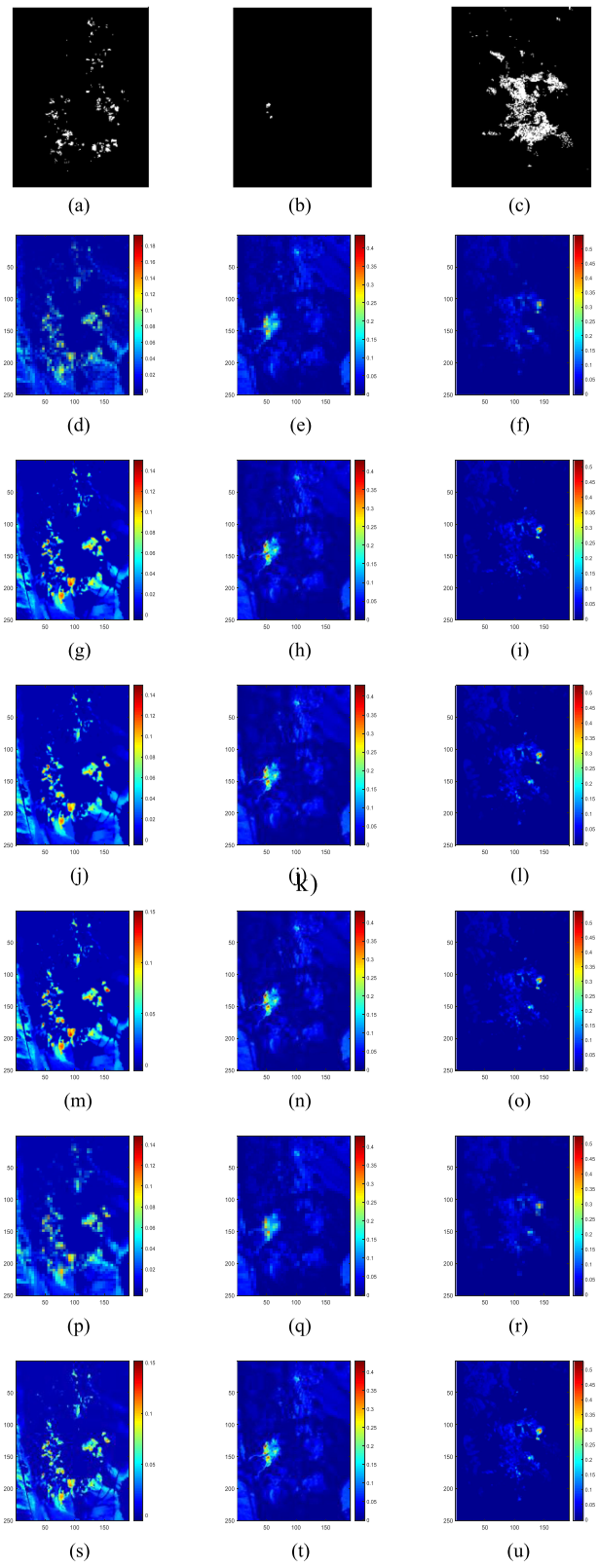

Fig. 11. Abundance images of USGS mineral map estimated by the six unmixing methods. The first row shows the distribution maps of Alunite, Buddingtonite, and Chalcedony (column 1–3) by Tricorder software. The second to the seventh row shows the estimated abundances images of the three minerals by CLSUnSAL, SUnSAL-TV, J-LASU, L1-L2 SUnSAL-TV, NLLRSU, and our method, respectively.

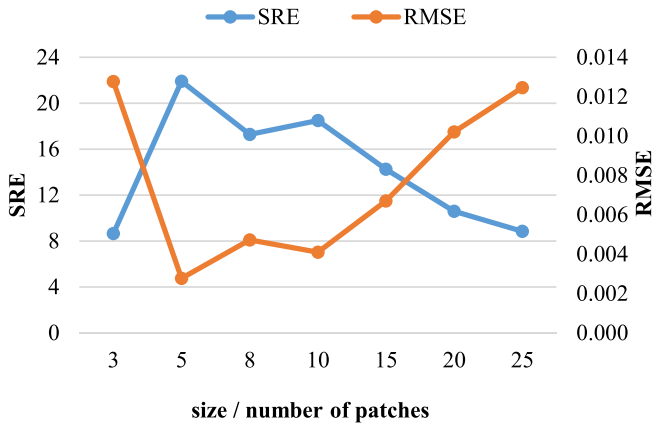

Fig. 12. SRE and RMSE values as a function of the size and number of patches.

J-LASU, l_1-l_2 SUnSAL-TV, NLLRSU, and WNLTDSU, respectively. From Fig. 11, it can be seen that CLSUnSAL has poor noise suppression and poor unmixing performance, and SUnSAL-TV causes over-smoothing in some regions, while WNLTDSU suppresses the noise and maintains the structural information best. The unmixing results of the WNLTDSU are also closer to the real abundance images than the results of the other methods, which reflects the superiority of the proposed method.

C. Discussion

The execution time of the six methods used on the DS1 and Cuprite dataset are summarized in Table IV. The six methods were implemented in MATLAB R2018b on a desktop computer with an Intel Core i7 (at 3.6 GHz) CPU and 8 GB of memory. Ten experiments were performed for each method, and the average time was taken as the running time of each method. It can be clearly seen that the proposed method consumes the most time among the six algorithms. The reason is that it takes much time to calculate the singular value decomposition. However, the proposed method, particularly at a strong noise level, suppresses the noise and maintains the structural information of the abundance images best. Moreover, for hyperspectral big data processing or real-time application, distributed parallel computing can be utilized to speed up the algorithm by dealing with the cubic patches.

In addition, the size and number of patches also need to be considered in experiments, as they affect the unmixing performances. Fig. 12 presents the changes in SRE and RMSE with the size and number of patches in DS1+. It explains that the SRE and RMSE results are best when the size and number of patches are both five. As the size and number of blocks increase, the unmixing performance gradually decreases. After several experiments, we found that using a $5 \times 5 \times 5$ size for each patch and five patches to form the patch group tensor for the low-rank tensor decomposition achieves good results on most datasets. Hence, we selected the $5 \times 5 \times 5$ size for each patch and five patches as the optimal parameters for all the data.

TABLE IV
EXECUTION TIME OF THE SIX METHODS (SECONDS/ITERATION)

Algorithms	CLSUnSAL [40]	SUnSAL-TV [45]	J-LASU [60]	l_1-l_2 SUnSAL-TV [74]	NLLRSU [75]	Our Method
DS1	0.09	0.33	1.51	0.34	2.89	3.30
Cuprite Dataset	0.22	0.62	2.87	0.66	5.76	7.03

V. CONCLUSION

We proposed a hyperspectral sparse unmixing method based on weighted nonlocal low-rank tensor decomposition regularization, which takes into account the spatial and spectral information, simultaneously. Based on the prior that the HSI has strong nonlocal similarity, several patches were combined to form a patch group tensor. The weighted nuclear norm was then applied to this patch group tensor to obtain the estimated abundance image. In addition, collaborative sparsity and TV regularization were also introduced in the proposed model to consider the spectral and spatial information of the abundance image. The proposed method was tested on two simulated datasets and a real hyperspectral dataset, and the results showed that the proposed method was superior to the state-of-the-art methods. In the future, we will consider implementing our algorithm on the GPU or cloud platform [77]–[79], to reduce the runtime and improve efficiency.

REFERENCES

[1] J. M. Bioucas-Dias, A. Plaza, G. Camps-Valls, P. Scheunders, N. M. Nasrabadi, and J. Chanussot, "Hyperspectral remote sensing data analysis and future challenges," *IEEE Geosci. Remote Sens. Mag.*, vol. 1, no. 2, pp. 6–36, Jun. 2013.

[2] L. Zhang, L. Zhang, D. Tao, X. Huang, and B. Du, "Compression of hyperspectral remote sensing images by tensor approach," *Neurocomputing*, vol. 147, pp. 358–363, Jan. 2015.

[3] L. Zhang, L. Zhang, B. Du, J. You, and D. Tao, "Hyperspectral image unsupervised classification by robust manifold matrix factorization," *Inf. Sci.*, vol. 485, pp. 154–169, Jun. 2019.

[4] Z. Wu, W. Zhu, J. Chanussot, Y. Xu, and S. Osher, "Hyperspectral anomaly detection via global and local joint modeling of background," *IEEE Trans. Signal Process.*, vol. 67, no. 14, pp. 3858–3869, Jul. 2019.

[5] Y. Chen, Y. Ge, G. B. M. Heuvelink, R. An, and Y. Chen, "Object-based superresolution land-cover mapping from remotely sensed imagery," *IEEE Trans. Geosci. Remote Sens.*, vol. 56, no. 1, pp. 328–340, Jan. 2018.

[6] H. Li, J. Liu, and H. Yu, "An automatic sparse pruning endmember extraction algorithm with a combined minimum volume and deviation constraint," *Remote Sens.*, vol. 10, no. 4, pp. 32, Apr. 2018.

[7] N. Xu, X. Geng, H. You, and Y. Cao, "A fully constrained linear unmixing method: Simplex regularization for hyperspectral imagery," *J. Infrared Millim. Waves*, vol. 35, no. 5, pp. 592–599, Oct. 2016.

[8] J. Yuan, Y. Zhang, and F. Gao, "An overview on linear hyperspectral unmixing," *J. Infrared Millim. Waves*, vol. 37, no. 5, pp. 553–571, Oct. 2018.

[9] Y. Gu and Y. Zhang, "Hyperspectral small target detection by combining kernel PCA with linear mixture model," *Chin. J. Electron.*, vol. 14, no. 1, pp. 130–134, Jan. 2005.

[10] D. Hong, N. Yokoya, J. Chanussot, and X. Zhu, "An augmented linear mixing model to address spectral variability for hyperspectral unmixing," *IEEE Trans. Image Process.*, vol. 28, no. 4, pp. 1923–1938, Apr. 2019.

[11] R. Heylen, M. Parente, and P. Gader, "A review of nonlinear hyperspectral unmixing methods," *IEEE J. Sel. Top. Appl. Earth Obs. Remote Sens.*, vol. 7, no. 6, pp. 1844–1868, Jun. 2014.

[12] Q. Wei, M. Chen, J. Y. Tourneret, and S. Godsill, "Unsupervised nonlinear spectral unmixing based on a multilinear mixing model," *IEEE Trans. Geosci. Remote Sens.*, vol. 55, no. 8, pp. 4534–4544, Aug. 2017.

[13] M. Tang, L. Gao, A. Marinoni, P. Gamba, and B. Zhang, "Integrating spatial information in the normalized P-linear algorithm for nonlinear hyperspectral unmixing," *IEEE J. Sel. Top. Appl. Earth Obs. Remote Sens.*, vol. 11, no. 4, pp. 1179–1190, Apr. 2018.

[14] M. Tang, B. Zhang, A. Marinoni, L. Gao, and P. Gamba, "Multiharmonic postnonlinear mixing model for hyperspectral nonlinear unmixing," *IEEE Geosci. Remote Sens. Lett.*, vol. 15, no. 11, pp. 1765–1769, Nov. 2018.

[15] C. Chang, Y. Li, and Y. Wang, "Progressive band processing of fast iterative pixel purity index for finding endmembers," *IEEE Geosci. Remote Sens. Lett.*, vol. 14, no. 9, pp. 1464–1468, Sep. 2017.

[16] I. Gueddi, O. Nasri, K. Benothman, and P. Dague, "Fault detection and isolation of spacecraft thrusters using an extended principal component analysis to interval data," *Int. J. Control Autom. Syst.*, vol. 15, no. 2, pp. 776–789, Apr. 2017.

[17] E. M. Sigurdsson, A. Plaza, and J. A. Benediktsson, "GPU implementation of iterative-constrained endmember extraction from remotely sensed hyperspectral images," *IEEE J. Sel. Top. Appl. Earth Obs. Remote Sens.*, vol. 8, no. 6, pp. 2939–2949, Jun. 2015.

[18] X. Li, X. Jia, L. Wang, and K. Zhao, "Reduction of spectral unmixing uncertainty using minimum-class-variance support vector machines," *IEEE. Geosci. Remote Sens. Lett.*, vol. 13, no. 9, pp. 1335–1339, Sep. 2016.

[19] Y. Chen, W. Xu, J. Zuo, and K. Yang, "The fire recognition algorithm using dynamic feature fusion and IV-SVM classifier," *Cluster Comput.*, vol. 22, no. 3, pp. 7665–7675, May 2019.

[20] Y. Chen, J. Xiong, W. Xu, and J. Zuo, "A novel online incremental and decremental learning algorithm based on variable support vector machine," *Cluster Comput.*, vol. 22, no. 3, pp. 7435–7445, May 2019.

[21] G. A. Licciardi, and F. D. Frate, "Pixel unmixing in hyperspectral data by means of neural networks," *IEEE. Trans. Geosci. Remote Sens.*, vol. 49, no. 11, pp. 4163–4172, Nov. 2011.

[22] M. Long and Y. Zeng, "Detecting iris liveness with batch normalized convolutional neural network," *Comput. Mater. Continua*, vol. 58, no. 2, pp. 493–504, 2019.

[23] D. Zeng, Y. Dai, F. Li, J. Wang, and A. Kumar, "Aspect based sentiment analysis by a linguistically regularized CNN with gated mechanism," *J. Intell. Fuzzy Syst.*, vol. 36, pp. 3971–3980, Apr. 2019.

[24] R. Meng, S. Rice, J. Wang, and X. Sun, "A fusion steganographic algorithm based on faster R-CNN," *Comput. Mater. Continua*, vol. 55, no. 1, pp. 1–16, Apr. 2018.

[25] Y. Tu, Y. Lin, J. Wang, and J. U. Kim, "Semi-supervised learning with generative adversarial networks on digital signal modulation classification," *Comput. Mater. Continua*, vol. 55, pp. 243–254, Jan. 2018.

[26] W. Wang, Y. Jiang, Y. Luo, J. Li, X. Wang, and T. Zhang, "An advanced deep residual dense network (DRDN) approach for image super-resolution," *Int. J. Comput. Int. Syst.*, vol. 12, no. 2, pp. 1592–1601, Dec. 2019.

[27] L. Xiang, X. Shen, J. Qin, and W. Hao, "Discrete multi-graph hashing for large-scale visual search," *Neural Process. Lett.*, vol. 49, no. 3, pp. 1055–1069, Jun. 2019.

[28] T. Zhu, Y. Lin, Y. Liu, W. Zhang, and J. Zhang, "Minority oversampling for imbalanced ordinal regression," *Knowl. Based Syst.*, vol. 166, pp. 140–155, Feb. 2019.

[29] S. Zhou, M. Ke, and P. Luo, "Multi-camera transfer GAN for person re-identification," *J. Vis. Commun. Image Represent.*, vol. 59, pp. 393–400, Feb. 2019.

[30] Y. Qian, F. Xiong, S. Zeng, J. Zhou, and Y. Tang, "Matrix-vector nonnegative tensor factorization for blind unmixing of hyperspectral imagery," *IEEE Trans. Geosci. Remote Sens.*, vol. 55, no. 3, pp. 1776–1792, Mar. 2017.

[31] X. Wang, Y. Zhong, L. Zhang, and Y. Xu, "Spatial group sparsity regularized nonnegative matrix factorization for hyperspectral unmixing," *IEEE Trans. Geosci. Remote Sens.*, vol. 55, no. 11, pp. 6287–6304, Nov. 2017.

[32] Z. Wu, J. Liu, S. Ye, L. Sun, and Z. Wei, "Optimization of minimum volume constrained hyperspectral image unmixing on CPU-GPU heterogeneous platform," *J. Real Time Image Process.*, vol. 15, no. 2, pp. 265–277, Aug. 2018.

[33] S. He, Z. Li, Y. Tang, Z. Liao, F. Li, and S. J. Lim, "Parameters compressing in deep learning," *Comput. Mater. Continua*, vol. 62, no. 1, pp. 321–336, 2019.

[34] Y. Song, G. Yang, H. Xie, D. Zhang, and X. Sun, "Residual domain dictionary learning for compressed sensing video recovery," *Multimed. Tools Appl.*, vol. 76, no. 7, pp. 10083–10096, Apr. 2017.

[35] Y. Xu, Z. Wu, J. Chanussot, and Z. Wei, "Joint reconstruction and anomaly detection from compressive hyperspectral images using mahalanobis distance-regularized tensor RPCA," *IEEE Trans. Geosci. Remote Sens.*, vol. 56, no. 5, pp. 2919–2930, May 2018.

[36] D. Wang, Z. Shi, and X. Cui, "Robust sparse unmixing for hyperspectral imagery," *IEEE Trans. Geosci. Remote Sens.*, vol. 56, no. 3, pp. 1348–1359, Mar. 2018.

[37] W. Tang, Z. Shi, Y. Wu, and C. Zhang, "Sparse unmixing of hyperspectral data using spectral a priori information," *IEEE. Trans. Geosci. Remote Sens.*, vol. 53, no. 2, pp. 770–783, Feb. 2015.

[38] S. Zhang, J. Li, K. Liu, C. Deng, L. Liu, and A. Plaza, "Hyperspectral unmixing based on local collaborative sparse regression," *IEEE. Geosci. Remote Sens. Lett.*, vol. 13, no. 5, pp. 631–635, May 2016.

[39] M. D. Iordache, J. M. Bioucas-Dias, and A. Plaza, "Sparse unmixing of hyperspectral data," *IEEE. Trans. Geosci. Remote Sens.*, vol. 49, no. 6, pp. 2014–2039, Jun. 2011.

[40] M. D. Iordache, J. M. Bioucas-Dias, and A. Plaza, "Collaborative sparse regression for hyperspectral unmixing," *IEEE. Trans. Geosci. Remote Sens.*, vol. 52, no. 1, pp. 341–354, Jan. 2014.

[41] C. Deng, S. Zhang, S. Wang, W. Tian, and Z. Wu, "Sparse hyperspectral unmixing based on smoothed l(0) regularization," *Infrared Phys. Technol.*, vol. 67, pp. 306–314, Nov. 2014.

[42] L. Sun, Z. Wu, L. Xiao, J. Liu, Z. Wei, and F. Dang, "A novel l(1/2) sparse regression method for hyperspectral unmixing," *Int. J. Remote Sens.*, vol. 34, no. 20, pp. 6983–7001, Oct. 2013.

[43] L. Sun, C. Ma, Y. Chen, H. J. Shim, Z. Wu, and B. Jeon, "Adjacent superpixel-based multiscale spatial-spectral kernel for hyperspectral classification," *IEEE J. Sel. Top. Appl. Earth Obs. Remote Sens.*, vol. 12, no. 6, pp. 1905–1919, 2019.

[44] D. Zhang, T. Yin, G. Yang, M. Xia, L. Li, and X. Sun, "Detecting image seam carving with low scaling ratio using multi-scale spatial and spectral entropies," *J. Vis. Commun. Image Represent.*, vol. 48, pp. 281–291, Oct. 2017.

[45] M. D. Iordache, J. M. Bioucas-Dias, and A. Plaza, "Total variation spatial regularization for sparse hyperspectral unmixing," *IEEE. Trans. Geosci. Remote Sens.*, vol. 50, no. 11, pp. 4484–4502, Nov. 2012.

[46] H. Liu, P. Sun, Q. Du, Z. Wu, and Z. Wei, "Hyperspectral image restoration based on low-rank recovery with a local neighborhood weighted spectral-spatial total variation model," *IEEE Trans. Geosci. Remote Sens.*, vol. 57, no. 3, pp. 1409–1422, Mar. 2019.

[47] J. Sigurdsson, M. O. Ulfarsson, and J. R. Sveinsson, "Blind hyperspectral unmixing using total variation and l(q) sparse regularization," *IEEE Trans. Geosci. Remote Sens.*, vol. 54, no. 11, pp. 6371–6384, Nov. 2016.

[48] R. Wang, H. Li, W. Liao, X. Huang, and W. Philips, "Centralized collaborative sparse unmixing for hyperspectral images," *IEEE J. Sel. Top. Appl. Earth Obs. Remote Sens.*, vol. 10, no. 5, pp. 1949–1962, May 2017.

[49] Y. Zhong, R. Feng, and L. Zhang, "Non-local sparse unmixing for hyperspectral remote sensing imagery," *IEEE J. Sel. Top. Appl. Earth Obs. Remote Sens.*, vol. 7, no. 6, pp. 1889–1909, Jun. 2014.

[50] R. Feng, Y. Zhong, and L. Zhang, "An improved nonlocal sparse unmixing algorithm for hyperspectral imagery," *IEEE Geosci. Remote Sens. Lett.*, vol. 12, no. 4, pp. 915–919, Apr. 2015.

[51] L. Sun *et al.*, "Low rank component induced spatial-spectral kernel method for hyperspectral image classification," *IEEE Trans. Circuits Syst. Video Technol.*, to be published, doi: 10.1109/TCSVT.2019.2946723.

[52] L. Sun, T. Zhan, Z. Wu, L. Xiao, and B. Jeon, "Hyperspectral mixed denoising via spectral difference-induced total variation and low-rank approximation," *Remote Sens.*, vol. 10, no. 12, Dec. 2018, Art. no. 1956.

[53] Y. Chang, L. Yan, and S. Zhong, "Hyper-Laplacian regularized unidirectional low-rank tensor recovery for multispectral image denoising," in *Proc. IEEE Conf. Comput. Vision Pattern Recognit.*, 2017, pp. 5901–5909.

[54] Y. Chen, R. Xia, Z. Wang, J. Zhang, K. Yang, and Z. Cao, "The visual saliency detection algorithm research based on hierarchical principle component analysis method," *Multimedia Tools Appl.*, vol. 75, pp. 16943–16958, 2019.

[55] Q. Liu, Z. Wu, L. Sun, Y. Xu, L. Du, and Z. Wei, "Kernel low-rank representation based on local similarity for hyperspectral image classification," *IEEE J. Sel. Top. Appl. Earth Obs. Remote Sens.*, vol. 12, no. 6, pp. 1920–1932, Jun. 2019.

[56] Y. Xu, Z. Wu, J. Chanussot, and Z. Wei, "Nonlocal patch tensor sparse representation for hyperspectral image super-resolution," *IEEE Trans. Image Process.*, vol. 28, no. 6, pp. 3034–3047, Jun. 2019.

[57] Y. Xu, Z. Wu, J. Chanussot, and Z. Wei, "Hyperspectral images super-resolution via learning high-order coupled tensor ring representation," *IEEE Trans. Neural Netw. Learn. Syst.*, to be published, doi: 10.1109/TNNLS.2019.2957527.

[58] J. Yang, L. Zhang, Y. Xu, and J. Yang, "Beyond sparsity: The role of L-1-optimizer in pattern classification," *Pattern Recognit.*, vol. 45, no. 3, pp. 1104–1118, Mar. 2012.

[59] J. Yang, D. Chu, L. Zhang, Y. Xu, and J. Yang, "Sparse representation classifier steered discriminative projection with applications to face recognition," *IEEE Trans. Neural Netw. Learn. Syst.*, vol. 24, no. 7, pp. 1023–1035, Jul. 2013.

[60] M. Rizkinia and M. Okuda, "Joint local abundance sparse unmixing for hyperspectral images," *Remote Sens.*, vol. 9, no. 12, Dec. 2017, Art. no. 1224.

[61] X. Zhang *et al.*, "Hyperspectral unmixing via low-rank representation with space consistency constraint and spectral library pruning," *Remote Sens.*, vol. 10, no. 2, Feb. 2018, Art. no. 339.

[62] D. Hong and X. Zhu, "SULoRA: Subspace unmixing with low-rank attribute embedding for hyperspectral data analysis," *IEEE J. Sel. Top. Signal Process.*, vol. 12, no. 6, pp. 1351–1363, Dec. 2018.

[63] D. Hong, N. Yokoya, J. Chanussot, and X. Zhu, "CoSpace: Common subspace learning from hyperspectral-multispectral correspondences," *IEEE Trans. Geosci. Remote Sens.*, vol. 57, no. 7, pp. 4349–4359, Jul. 2019.

[64] D. Hong, N. Yokoya, N. Ge, J. Chanussot, and X. Zhu, "Learnable manifold alignment (LeMA): A semi-supervised cross-modality learning framework for land cover and land use classification," *ISPRS J. Photogramm. Remote Sens.*, vol. 147, pp. 193–205, Jan. 2019.

[65] T. G. Kolda and B. W. Bader, "Tensor decompositions and applications," *SIAM Rev.*, vol. 51, no. 3, pp. 455–500, Sep. 2009.

[66] N. Dobigeon, S. Moussaoui, M. Coulon, J. Y. Tourneret, and A. O. Hero, "Joint Bayesian endmember extraction and linear unmixing for hyperspectral imagery," *IEEE Trans. Signal Process.*, vol. 57, no. 11, pp. 4355–4368, Nov. 2009.

[67] T. Cai and A. Zhang, "Sharp RIP bound for sparse signal and low-rank matrix recovery," *Appl. Comput. Harmon. Anal.*, vol. 35, no. 1, pp. 74–93, Jul. 2013.

[68] Q. Qu, N. M. Nasrabadi, and T. D. Tran, "Abundance estimation for bilinear mixture models via joint sparse and low-rank representation," *IEEE. Trans. Geosci. Remote Sens.*, vol. 52, no. 7, pp. 4404–4423, Jul. 2014.

[69] K. Dabov, A. Foi, V. Katkovnik, and K. Egiazarian, "Image denoising by sparse 3-D transform-domain collaborative filtering," *IEEE. Trans. Image Process.*, vol. 16, no. 8, pp. 2080–2095, Aug. 2007.

[70] J. Eckstein and D. P. Bertsekas, "On the Douglas–Rachford splitting method and the proximal point algorithm for maximal monotone operators," *Math. Program.*, vol. 55, no. 1/3, pp. 293–318, 1992.

[71] S. J. Wright, R. D. Nowak, and M. A. T. Figueiredo, "Sparse reconstruction by separable approximation," *IEEE. Trans. Signal Process.*, vol. 57, no. 7, pp. 2479–2493, Jul. 2009.

[72] P. P. Vinchurkar, S. V. Rathkanthiwar, and S. M. Kakde, "HDL implementation of DFT architectures using winograd fast fourier transform algorithm," in *Proc. 5th Int. Conf. Commun. Syst. Netw. Technologies*, Gwalior, India, 2015, pp. 397–401.

[73] P. L. Combettes and V. R. Wajs, "Signal recovery by proximal forward-backward splitting," *Multiscale Model. Simul.*, vol. 4, no. 4, pp. 1168–1200, 2005.

[74] L. Sun, W. Ge, Y. Chen, J. Zhang, and B. Jeon, "Hyperspectral unmixing employing l(1)-l(2) sparsity and total variation regularization," *Int. J. Remote Sens.*, vol. 39, no. 19, pp. 6037–6060, Oct. 2018.

[75] Y. Zheng, F. Wu, H. J. Shim, and L. Sun, "Sparse unmixing for hyperspectral image with nonlocal low-rank prior," *Remote Sens.*, vol. 11, no. 24, 2019, Art. no. 2897.

[76] R. N. Clark *et al.*, "USGS Digital Spectral Library Splib06a," Report 231, Reston, VA, USA, 2007. [Online]. Available: https://speclab.cr.usgs.gov/spectral.lib06

[77] Y. Jiang, M. Zhao, C. Hu, L. He, H. Bai, and J. Wang, "A parallel FP-growth algorithm on World Ocean Atlas data with multi-core CPU," *J. Supercomput.*, vol. 75, no. 2, pp. 732–745, Feb. 2019.

[78] Z. Wu *et al.*, "GPU parallel implementation of spatially adaptive hyperspectral image classification," *IEEE J. Sel. Top. Appl. Earth Obs. Remote Sens.*, vol. 11, no. 4, pp. 1131–1143, Apr. 2018.

[79] Z. Wu, Y. Li, A. Plaza, J. Li, and Z. Wei, "Parallel and distributed dimensionality reduction of hyperspectral data on cloud computing architectures," *IEEE J. Sel. Top. Appl. Earth Obs. Remote Sens.*, vol. 9, no. 6, pp. 2270–2278, Jun. 2016.

Le Sun (Member, IEEE) was born in Jiangsu, China, in 1987. He received the B.S. degree from the School of Science, Nanjing University of Science and Technology (NJUST), Nanjing, China, in 2009, where he obtained the Ph.D. degree from the School of Computer Science and Engineering in 2014.

He was doing research in the field of multi-images fusion based on sparse dictionary learning and compressive sensing as a Postdoctoral Researcher with the Digital Media Laboratory of the School of Electronic and Electrical Engineering, Sungkyunkwan University, Seoul, South Korea, from September 2015 to August 2018. He is currently an Associate Professor with the Nanjing University of Information Science and Technology. His research interests include sparse representation and compressive sensing, especially in the field of hyperspectral image processing.

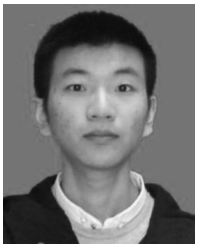

Feiyang Wu is a Graduate Student with the School of Computer and Software, Nanjing University of Information Science and Technology, Nanjing, China.

His current research interests include image processing, especially for hyperspectral image unmixing.

Tianming Zhan (Member, IEEE) received the B.S. and M.S. degrees from the School of Mathematics and Statistics, Nanjing University of Information Science and Technology, Nanjing, China, in 2006 and 2009, respectively, and the Ph.D. degree with the School of Computer Science and Engineering, Nanjing University of Science and Technology, in 2013.

He is currently an Associate Professor with the School of Information and Engineering, Nanjing Audit University, Nanjing, China. His research interests include medical image processing, hyperspectral image processing, machine learning, and data analysis.

Wei Liu received the B.S. and M.S. degrees in computer science from Yangzhou University, Yangzhou, China, in 2004 and 2007, respectively, and the Ph.D. degree from the Department of Computer Science from the Nanjing University of Aeronautics and Astronautics, Nanjing, China, in 2010.

She was a Visiting Scholar with Sungkyunkwan University, Seoul, South Korea. She is currently a Full Professor with the Institute of Information Science and Technology, Yangzhou University. Her current research interests include complex network, data mining, and bioinformatics.

Jin Wang received the B.S. and M.S. degrees from the Nanjing University of Posts and Telecommunication, Nanjing, China, in 2002 and 2005, respectively, and the Ph.D. degree from Kyung Hee University, Seoul, South Korea, in 2010.

He is currently a Professor with the Changsha University of Science and Technology, Changsha, China and the Fujian University of Technology, Fuzhou, China. His research interests mainly include routing protocol and algorithm design, and performance evaluation for wireless ad hoc and sensor networks.

Dr. Wang is also a member of ACM.

Byeungwoo Jeon (Senior Member, IEEE) received the B.S. degree (Magna Cum Laude) in 1985, the M.S. degree in 1987, in electronics engineering from Seoul National University, Seoul, South Korea, and the Ph.D. degree in electrical engineering from Purdue University, West Lafayette, IN, USA, in 1992.

From 1993 to 1997, he was in the Signal Processing Laboratory, Samsung Electronics, Suwon, South Korea, where he conducted research and development into video compression algorithms, the design of digital broadcasting satellite receivers, and other MPEG-related research for multimedia applications. Since September 1997, he has been with the Faculty of the School of Electronic and Electrical Engineering, Sungkyunkwan University, Seoul, South Korea, where he is currently a Full Professor. He served as Project Manager of Digital TV and Broadcasting in the Korean Ministry of Information and Communications from March 2004 to February 2006, where he supervised all digital TV-related R&D in South Korea. He has authored and coauthored many papers in the areas of video compression, pre/postprocessing, and pattern recognition. His research interests include multimedia signal processing, video compression, statistical pattern recognition, and remote sensing.

Dr. Jeon was a recipient of the 2005 IEEK Haedong Paper Award in Signal Processing Society, South Korea. He is a member of Tau Beta Pi and Eta Kappa Nu. He is also a member of SPIE, IEEK, KICS, and KSOBE.